Reduced-Complexity Joint Frequency, Timing and Phase Recovery for PAM Based CPM Receivers

2009
Sayak Bose

Submitted to the graduate degree program in Electrical Engineering and Computer Science and the Graduate Faculty of the University of Kansas in partial fulfillment of the requirements for the degree of Master of Science.

Thesis Committee:

Dr. Erik Perrins: Chairperson

Dr. K. Sam Shanmugan

Dr. Shannon Blunt

Date Defended

The Thesis Committee for Sayak Bose certifies
that this is the approved version of the following thesis:

Reduced-Complexity Joint Frequency, Timing, and Phase Recovery for PAM Based CPM Receivers

Committee:

_____

Chairperson

_____

_____

_____

Date Approved

To my mom

Acknowledgements

I would like to acknowledge and thank people who have supported me in this thesis. I thank Dr. Perrins, my advisor for his valuable guidance and inputs all through my thesis. I would also like to thank Dr. Shanmugan and Dr. Blunt for being on my thesis committee and reviewing this thesis document. I would like to thank the department of Electrical Engineering and Computer Science at The University of Kansas for all its support.

I would like to thank my mom for her unconditional love and affection. She has been my source of inspiration in important phases of my life. I would also like to thank my Aunts Juthika and Minati and Uncles Aloke and Animesh for their kind support to my family.

I thank all my friends here in Lawrence, Kansas, and in India, for the fun and support I have had all my life.

Abstract

In this thesis, we present a reduced-complexity decision-directed *joint* timing and phase recovery method for continuous phase modulation (CPM). Using a simple linear modulation—pulse amplitude modulation (PAM)—representation of CPM, more popularly known as the Laurent representation of CPM, we develop formulations of a PAM based *joint* timing error detector (TED) and a phase error detector (PED). We consider the general M-ary single-h CPM model in our developments and numerical examples. We show by analysis and computer simulations that the PAM based error detector formulations have characteristics similar to the *conventional* (i.e., non-PAM) formulations and they render reliable performance when applied to specific CPM examples; in fact, we show the error detectors are able to perform close to the theoretical limit given by the modified Cramer-Rao bound (MCRB) and able to provide a bit error rate (BER) close to the theoretical value. Also, we investigate the false lock problem in M-ary CPMs and are able to obtain much improved performance over conventional CPM detectors with our PAM based method. Furthermore, the PAM based receivers perform well in the presence of a large frequency offset (on the order of the symbol rate) and are, in general, much more resistant to small carrier frequency variations compared to conventional CPM receivers. We use an existing PAM based frequency difference detector (FDD) for a large carrier frequency recovery. As such, the proposed method of combining the error detectors (FDD, TED and PED) provides important synchronization components for *jointly* recovering the respective signal attribute offsets (i.e, carrier frequency, symbol timing and carrier phase) for reduced-complexity PAM based CPM receivers, which have been missing up to this point.

Contents

List of Figures

List of Tables

Chapter 1

Introduction

Continuous phase modulation (CPM) [1], as the name suggests, is a type of digital phase modulation where the phase change is done continuously instead of abruptly (viz. Quadrature Phase Shift Keying or QPSK) over time in order to reduce out of band power requirement. It is a jointly power and bandwidth efficient digital modulation scheme. In long range telemetry applications, its constant-envelope nature is beneficial as it allows simple (inexpensive) transmitters and high efficiency in converting source power into radiated power. In other power-limited (i.e. battery powered) mobile applications such as Global System for Mobile (GSM), this feature is also critical. The CPM transmitters are simple to build because the analog power amplifiers can be made to work in the *saturation* zone all the time thereby discarding the need for any complex adaptive gain compensations. However, since the modulation itself is nonlinear in nature, its receivers are often complex and its deployment beyond the family of minimum-shift keying (MSK)-type versions has been limited. Also, the nonlinear nature of the modulation makes synchronization more difficult.

The most popular method of dealing with the nonlinearity of CPM has been to "linearize" it with a pulse amplitude modulation (PAM) representation. This method of

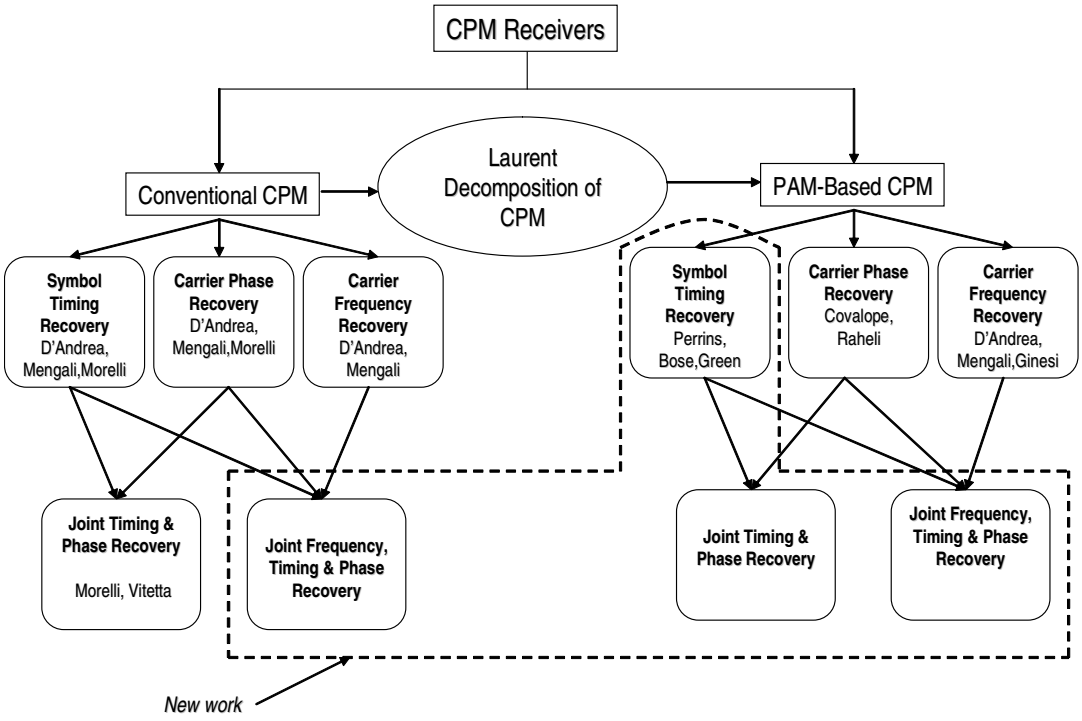

Figure 1.1. Overview of CPM receiver synchronization related research work.

"linearizing" CPM was first proposed for binary CPMs in the widely known paper by Laurent [2]. This method has since been extended to M-ary single-h CPM [3], M-ary multi-h CPM [4], and cases such as integer modulation index [5], data-dependent pulses [6] etc. This linearization of CPM made way for the design of reduced-complexity detectors [7–9], carrier phase recovery [8] and carrier frequency recovery [10].

The problems of symbol timing and carrier phase recovery for CPM have received persistant attention over the years. As we can see from Figure. 1.1 the following related works in CPM are of importance: In [11], a novel NDA timing recovery scheme was developed which was slow in nature but free from any false lock problems. In [12], another decision-directed (DD) joint phase and timing recovery scheme was developed which was much faster than the one based on NDA recovery but suffers from the false

lock problem. Both these algorithms used the *conventional* CPM models. In [13], a joint time and phase synchronization scheme was proposed based on nonorthogonal exponential expansions and Kalman filtering. None of these previous studies for CPM timing and phase recovery were based on the reduced-complexity PAM representation of CPM.

The PAM representation was applied to timing recovery in [14], but only for the special case of MSK-type signals, not for CPM in general. The algorithm for reduced-complexity PAM based phase recovery was first presented in [8] but without the consideration of any non-synchronized symbol timing clock. In [12] frequency detectors for the PAM representation of CPM were discussed but no symbol timing and carrier phase offsets were taken into consideration. An interesting similarity of all these previous studies involving the PAM representation of CPM is that they are not comprehensive in the following two ways:

1. They did not consider the case of PAM based reduced-complexity *joint* timing and phase recovery for CPMs.

2. They did not present any concrete observations on the performance of timing or phase recovery algorithms under a large carrier frequency shift which is a common problem in any long range telemetry applications.

In this thesis, we first attempt to unify all the previous work done on the PAM representation of CPM to solve the problem of *joint* symbol timing and carrier phase recovery without any offset in carrier frequency. Next, we cover the most general case of *joint* timing and phase recovery for the PAM based model under a large carrier frequency offset. This necessitates a non-data-aided (NDA) carrier frequency recovery [10] before timing and phase recovery can be attempted. We derive the formulation for a PAM based timing error detector (TED) and use the existing phase error detector (PED) and

frequency difference detector (FDD) formulations in order to present a comprehensive evaluation of their performance against their *conventional* CPM counterparts in terms of the error tracking efficiency and the bit error probability. The proposed decision-directed *joint* PAM-based frequency, timing and phase recovery scheme is valid for any CPM. The PAM-based TED, PED and FDD can have different arrangements of the front-end matched filters (MFs). We use common binary and M-ary single-h CPMs as case studies for the proposed approach although this can be easily extended to the more general case of M-ary multi-h PAM based CPM receivers.

Furthermore, we expand on the work done in [9] into reduced-complexity noncoherent detection of our proposed PAM based receivers for CPM as this is very useful when the carrier frequency offset is large making coherent detection difficult.

Finally, we revisit the serious problem of false locks that is often suffered by M-ary partial-response CPMs. In [11], a NDA false lock recovery was described. Although, this eliminates the false lock problem, but it is very slow in acquiring the lock and adds extra noise to the system. We propose an easier and faster false lock recovery solution for M-ary CPMs. We show by simulations that a PAM based noncoherent TED with a single pulse is most suitable for accurately determining the timing lock. As the number of PAM components in the TED increases, its lock detection capability goes down making the probability of false locks higher. We also observe that a small amount of frequency offset is helpful for both conventional and PAM based CPM systems to reduce the possibility of false lock significantly. A comparative study on the false lock problem involving a PAM based CPM and its corresponding conventional form is presented in Chapter 6 to demonstrate the effectiveness of the solution.

Chapter 2

Signal Model

2.1 Conventional CPM Model

The conventional CPM signal model is given in [1]. It has a complex envelope of the form

$$s(t;\boldsymbol{\alpha}) \triangleq \sqrt{\frac{E_s}{T_s}} \exp\{j\psi(t;\boldsymbol{\alpha})\} \tag{2.1}$$

where E_s is the symbol energy and T_s is the symbol duration. The phase of the signal is given by

$$\psi(t;\boldsymbol{\alpha}) \triangleq 2\pi \sum_i \alpha_i h_{\underline{i}} q(t - iT_s) \tag{2.2}$$

where $\boldsymbol{\alpha} \triangleq \{\alpha_i\}$ is a sequence of M-ary data symbols carrying $m = \log_2(M)$ bits and $\{h_i\}_{i=0}^{N_h-1}$ is a set of N_h *modulation indexes*. The underlined subscript notation in (2.2) is defined as modulo-N_h, i.e. $\underline{i} \triangleq i \bmod N_h$. When $N_h = 1$ we have *single-h* CPM, which is the most common case. When $N_h \geq 1$ we have the less-common *multi-h* CPM case. Henceforth, we will consider only the single-h case and all our examples in Chapter 6 are based on single-h CPMs. We assume that h is a rational number, i.e., $h = \frac{k}{p}$, with k and p mutually prime integers. We write the phase $\psi(t;\boldsymbol{\alpha})$ for the

single-h case as

$$\psi(t;\boldsymbol{\alpha}) \triangleq 2\pi h \sum_i \alpha_i q(t - iT_s). \tag{2.3}$$

The *phase response* $q(t)$ is obtained by integrating the *frequency pulse* $f(t)$ over a time duration of L symbol times. Before integration, $f(t)$ is normalized to have an area of $1/2$, irrespective of the pulse shape used. Therefore, $q(t)$ can be defined as

$$q(t) = \begin{cases} 0, & t < 0 \\ \displaystyle\int_0^t f(\tau)d\tau, & 0 \le t \le LT_s. \\ \frac{1}{2}, & t \ge LT_s \end{cases},$$

When $L = 1$ the signal is *full-response* and when $L > 1$ the signal is *partial-response*. Some common pulse shapes are length-LT_s rectangular (LREC), length-LT_s raised-cosine (LRC), and Gaussian, which are all defined in [15, p. 119]. Using the fact that $h = \frac{k}{p}$ and $q(t) = \frac{1}{2}$ for $t \ge LT_s$, the phase $\psi(t;\boldsymbol{\alpha})$ in (2.3) can be further decomposed into two parts as

$$\psi(t;\boldsymbol{\alpha}) = \eta(t;\mathbf{c}_n) + \phi_{n-L}, \qquad nT_s \le t < (n+1)T_s, \tag{2.4}$$

where

$$\eta(t;\mathbf{c}_n) \triangleq 2\pi h \sum_{i=n-L+1}^{n} \alpha_i q(t - iT_s),$$

$$\mathbf{c}_n \triangleq [\alpha_{n-L+1}, \cdots, \alpha_{n-1}, \alpha_n], \tag{2.5}$$

and

$$\phi_{n-L} \triangleq \pi h \sum_{i=0}^{n-L} \alpha_i \bmod 2\pi. \tag{2.6}$$

In the above equations, $\mathbf{c}_n$ is the *correlative state vector*, ϕ_{n-L} is the *phase state*, and n is the *current symbol index*. For rational modulation indexes, the phase states are drawn from a *finite* alphabet of p points evenly distributed around the unit circle when k is even and $2p$ points when k is odd:

$$\phi_{n-L} = \begin{cases} \frac{\pi}{p}\left[k\sum_{-\infty}^{n-L}\alpha_i\right]_{\text{mod } p}, & (\text{even } k) \\ \frac{\pi}{p}\left[k\sum_{-\infty}^{n-L}\alpha_i\right]_{\text{mod } 2p}, & (\text{odd } k) \end{cases},$$

Therefore, the signal in (2.4) can be represented by a phase trellis of $N_{\text{S}} = pM^{L-1}$ states for even k and $N_{\text{S}} = 2pM^{L-1}$ for odd k. Each branch is associated with a unique value of the *branch vector* $[\phi_{n-L}, \mathbf{c}_n]$.

2.2 PAM Based CPM model

In his paper [2], Laurent showed that the right-hand side of (2.1) can be represented as a superposition of data-modulated pulses for the special case of binary ($M = 2$) single-h CPM with non-integer modulation index. This has been further extended to the cases mentioned in Chapter 1. For our development, we restrict ourselves to the cases considered in [2, 3] although it can be extended to cases described in [4–6]. Using the PAM based model for M-ary single-h CPM, the right-hand side of (2.1) can be *exactly* represented as [3]

$$s(t;\boldsymbol{\alpha}) = \sqrt{\frac{E_s}{T_s}}\sum_{k=0}^{N-1}\sum_{i} b_{k,i}\, g_k(t - iT_s) \tag{2.7}$$

where the number of PAM components is $N = 2^{P(L-1)}(M-1)$ and $P = \log_2(M)$ when the alphabet size M is an integer power of 2. The pseudo-symbols $\{b_{k,i}\}_{k=0}^{N-1}$ and the pulses $g_k(t)$ can be obtained by multiplying P binary PAM waveforms, each of

which has the form

$$s_b(t;\boldsymbol{\alpha}) = \sum_{k=0}^{Q-1} \sum_{i} a_{k,i} c_k(t - iT_s) \tag{2.8}$$

where the set of Q signal pulses $c_k(t)$ can be found from the phase response of the CPM scheme. More detailed definitions of the pseudo-symbols can be found in [2, 3] for binary and M-ary cases with general multi-h cases described in [4]. The important fact to note about the pseudo-symbols is that the nonlinearity of conventional CPM is now isolated in the pseudo-symbols. Also, the important characteristics of the PAM signal pulses $\{g_k(t)\}_{k=0}^{N-1}$ are that they vary greatly in amplitude and in duration, having the total signal energy unevenly distributed among them. Their definitions can be found in [2–4] for the binary, M-ary, and multi-h cases. In general, the k-th pulse has a duration of D_k symbol times, where D_k is an integer in the range $1 \leq D_k \leq L+1$. The strongest energy pulse has the longest duration. Following the definition of the pseudo-symbols, the phase state ϕ_{i-L} can be factored out of $b_{k,i}$, leaving a term that is a function of the correlative state vector $\mathbf{c}_i$, i.e.

$$s(t;\boldsymbol{\alpha}) = \sqrt{\frac{E_s}{T_s}} \sum_{i} e^{j\phi_{i-L}} \sum_{k=0}^{N-1} b_k(\mathbf{c}_i) g_k(t - iT_s). \tag{2.9}$$

Equation (2.9) emphasizes the *PAM complexity reduction principle*, which has been used to formulate reduced-complexity detectors [7]. The complexity reduction is done in two ways. First, the facts that the pulses with the largest amplitudes also have the longest durations (i.e. the most energy), and that there are only a few such pulses [2, 3] are taken into consideration. The longest duration pulse indexes are grouped together in the subset $\mathcal{K}$, where $\mathcal{K} \subseteq \{0, 1, \cdots, N-1\}$ and has $|\mathcal{K}|$ elements. The reduced number of pulses are now used for the matched filter (MF) bank and the synchronization error detectors (TED, PED and FDD).

The second complexity-reduction step is to shorten the length of the correlative state vectors, which has the net effect of reducing the number of trellis states. It is observed that, with the remaining pseudo-symbols $\{b_k(\mathbf{c}_i)\}_{k\in\mathcal{K}}$, it is still possible to factor out additional data symbols, starting with α_{i-L+1}, which *shortens* the correlative state vector and thereby reduces the number of trellis states in the Viterbi based detector [7]. The full correlative state vector $\mathbf{c}_n$ in (2.5) contains L elements, whereas the shortened version $\mathbf{c}'_n$ contains only $L' \leq L$ elements. The $\{\alpha_i\}_{i=n-L+1}^{n-L'}$ elements that are removed from $\mathbf{c}'_n$ are *absorbed* into the phase state $\phi_{n-L'}$. The value of L' is determined by the choice of $\mathcal{K}$. Usually the duration of the *shortest PAM pulse* is used to fix the value of $\mathcal{K}$. Although there are some intricate inner-workings involved, it was shown in [9] that L' can be identified via the relation

$$L' = \begin{cases} L - D_{\text{min}} + 1, & D_{\text{min}} < L+1 \\ 1, & D_{\text{min}} = L+1 \end{cases}, \text{ where } D_{\text{min}} \triangleq \min_{k\in\mathcal{K}} D_k.$$

Therefore, this two fold concept outlined above is used to formulate reduced-complexity PAM based detectors and are used in conjuction with decision-directed symbol detection, timing and phase recovery and NDA frequency recovery discussed in the next chapter.

Chapter 3

PAM Based Detection and Signal Recovery

In this chapter, we first present coherent PAM based symbol detection and timing recovery using the complexity-reduction concepts developed in the previous chapter. Next, we present, in brief, the formulations for noncoherent detection derived in [16]. Finally, we illustrate the formulations for PAM based methods of phase recovery and frequency recovery which are originally derived in detail in [8] and in [10] respectively. In the subsequent chapters, we will use these algorithms to find a way to "fuse" them together to find formulations for *joint* frequency, phase and timing recovery.

To present the algorithms, we fix a generic signal model that is observed at the receiver as

$$r(t) = s(t - \tau; \boldsymbol{\alpha}) e^{(j\theta + j2\pi\nu t)} + w(t) \tag{3.1}$$

where $w(t)$ is complex-valued additive white Gaussian noise (AWGN) with zero mean and power spectral density N_0. The variables $\boldsymbol{\alpha}$, τ, θ, and ν represent the data symbols, the symbol timing offset, the carrier/channel phase offset and the carrier frequency

offset respectively. In practice, all of these variables are unknown to the receiver and must be recovered. In order to simplify the analysis of phase, timing and frequency recovery, we will make several assumptions without disturbing the generality of (3.1).

3.1 Receiver with Explicit Recovery of Symbol Sequence, Symbol Timing and Carrier/Channel Phase

We follow maximum likelihood methods to recover all the signal attributes mentioned. The idea is to first detect the symbol sequence, and then use this symbol sequence to direct the PLL to lock on to the correct timing and phase. For illustration purpose, however, while describing recovery of one attribute we will assume that all the other attributes (including the carrier frequency offset in (3.1)) are known. We will discuss about the frequency recovery in 3.3 as it is recovered in a non-data-aided fashion.

3.1.1 Sequence Detection

The symbol sequence $\boldsymbol{\alpha}$ is recovered using maximum likelihood sequence detection (MLSD). Following the assumptions stated before the received signal takes the form

$$r(t) = s(t; \boldsymbol{\alpha}) + w(t). \tag{3.2}$$

Here, we carry out the analysis for a known timing, phase and frequency offset. According to [1], the symbol sequence is determined by maximizing the log-likelihood function for the hypothesized symbol sequence $\tilde{\boldsymbol{\alpha}}$ over the observation interval $0 \leq t \leq L_0 T_s$

$$\Lambda(\boldsymbol{r}|\tilde{\boldsymbol{\alpha}}) = \text{Re}\left\{\int_0^{L_0 T_s} r(t) s^*(t; \tilde{\boldsymbol{\alpha}})\, dt\right\} \tag{3.3}$$

where $(\cdot)^*$ denotes the complex conjugate. Using $\mathcal{K}$ from (2.9) in (3.3), results in the form

$$\Lambda(\boldsymbol{r}|\tilde{\boldsymbol{\alpha}}) \approx \text{Re}\left\{\int_0^{L_0T_s} r(t)\sum_i e^{-j\tilde{\phi}_{i-L'}}\sum_{k\in\mathcal{K}} b_k^*(\tilde{\mathbf{c}}_i')g_k(t-iT_s)dt\right\}.$$

Since integration and summation are both linear operations, they are interchangable; this results in

$$\Lambda(\boldsymbol{r}|\tilde{\boldsymbol{\alpha}}) \approx \sum_i^{L_0-1}\text{Re}\left\{e^{-j\tilde{\phi}_{i-L'}}\int_0^{L_0T_s} r(t)\sum_{k\in\mathcal{K}} b_k^*(\tilde{\mathbf{c}}_i')g_k(t-iT_s)dt\right\}.$$

This can be written in a compact form as

$$\Lambda(\boldsymbol{r}|\tilde{\boldsymbol{\alpha}}) \approx \sum_{i=0}^{L_0-1}\text{Re}\big\{y_i(\tilde{\mathbf{c}}_i',\tilde{\phi}_{i-L'})\big\} \tag{3.4}$$

Equation (3.4) can be maximized efficiently using the Viterbi Algorithm (VA), e.g. [1, Ch. 7]. The *metric increment* through each step of the VA is $y_i(\tilde{\mathbf{c}}_i',\tilde{\theta}_{i-L'})$ and has the following form:

$$y_i(\tilde{\mathbf{c}}_i',\tilde{\phi}_{i-L'}) \triangleq e^{-j\tilde{\phi}_{i-L'}}\sum_{k\in\mathcal{K}} b_k^*(\tilde{\mathbf{c}}_i')x_{k,i}. \tag{3.5}$$

The time-reversed PAM pulses $\{g_k(-t)\}_{k\in\mathcal{K}}$ serve as the impulse responses of the MF bank [7, 9]. The outputs can be obtained by correlating the MF impulse response with the received signal

$$x_{k,i} \triangleq \int_{iT_s}^{(i+D_k)T_s} r(t)g_k(t-iT_s)\,dt \tag{3.6}$$

The matched filter output is sampled at variable instants of $t = (i+D_k)T_s$. The implementation of the MF bank requires a delay of LT_s in order to make the longest impulse response causal. Let us take a moment to observe some of the key attributes of (3.5) and (3.6):

1. The interval of integration in (3.6) spans *multiple* symbol intervals to account for the variable lengths of the MF pulses.

2. For the current time step n within the VA, the metric increment $y_n(\tilde{\mathbf{c}}'_n, \tilde{\phi}_{n-L'})$ produces a branch metric update of

$$\lambda(n) = \lambda(n-1) + y_n(\tilde{\mathbf{c}}'_n, \tilde{\phi}_{n-L'}) \tag{3.7}$$

   Also, y_n a function only of the current *shortened* branch vector $[\tilde{\mathbf{c}}'_n, \tilde{\phi}_{n-L'}]$ and therefore requires a trellis of only $pM^{L'-1}$ or $2pM^{L'-1}$ states depending on whether k in the modulation index h is even or odd respectively. This is the state complexity reduction principle discussed in Chapter 2.

3.1.2 Timing Recovery and PAM Based Timing Error Detector Implementation

We now look into the data-aided recovery of τ, in which we assume that $\boldsymbol{\alpha}$ is exactly known. This is one of the major contributions of this thesis, as shown in Figure 1.1. These results also appear in [17]. The received signal is of the form

$$r(t) = s(t - \tau; \boldsymbol{\alpha}) + w(t). \tag{3.8}$$

Using the same conditional likelihood function defintions in Section 3.1.1, it can be easily shown that that the likelihood function for a hypothesized timing value $\tilde{\tau}$ is

$$\Lambda(\boldsymbol{r}|\tilde{\tau}) = \mathrm{Re}\left\{ \int_0^{L_0 T_s} r(t) s^*(t - \tilde{\tau}; \boldsymbol{\alpha})\, dt \right\}. \tag{3.9}$$

The maximum of $\Lambda(\boldsymbol{r}|\tilde{\tau})$ with respect to $\tilde{\tau}$ is obtained by setting the partial derivative of (3.9) with respect to $\tilde{\tau}$ equal to zero,

$$\text{Re}\left\{-\int_0^{L_0 T_s} r(t)\dot{s}^*(t-\tilde{\tau};\boldsymbol{\alpha})\,dt\right\} = 0 \tag{3.10}$$

where $\dot{s}(t)$ is the derivative of $s(t)$ with respect to time t, which leads to differentiating (3.5). Thus, the TED formulation parallels (3.4)–(3.6) yielding

$$\sum_{i=0}^{L_0-1} \text{Re}\left\{\dot{y}_i(\mathbf{c}_i, \phi_{i-L}, \tilde{\tau})\right\} = 0 \tag{3.11}$$

where the TED increment $\dot{y}_i(\mathbf{c}_i, \phi_{i-L}, \tilde{\tau})$ is given by

$$\dot{y}_i(\mathbf{c}_i, \theta_{i-L}, \tilde{\tau}) = \sum_{k\in\mathcal{K}_{\text{TED}}} b^*_{k,i}\dot{x}_{k,i}(\tilde{\tau}) \tag{3.12}$$

This TED increment could also be formulated with the shortened value L', i.e. $\dot{y}_i(\mathbf{c}'_i, \phi_{i-L'}, \tilde{\tau})$. $\dot{x}_{k,i}(t)$ is the output of the received signal correlated with the time derivative of the matched filter and can be shown as

$$\dot{x}_{k,i}(\tilde{\tau}) \triangleq \int_{\tau+iT_s}^{\tau+(i+D_k)T_s} r(t)\dot{g}_k(t-\tilde{\tau}-iT_s)\,dt. \tag{3.13}$$

A discrete-time differentiator is used to implement $\dot{x}_{k,i}(\tilde{\tau})$, which can be found in [18]. Some important observations made in formulating the solution to (3.11) are listed below:

1. Decision-directed timing recovery can be practically realized if the decisions from the VA are applied to direct the TED instead of the actual data symbols.

2. Satisfactory tracking performance can be achieved by using a different number of

PAM components (usually less) in the TED, $\mathcal{K}_{\text{TED}}$, than what is used for sequence detection, $\mathcal{K}$. This reduces the number of filters needed to support the TED.

The solution to (3.11) (i.e., the value of $\tilde{\tau}$ that causes the left-hand side of the equations to vanish) is obtained in an adaptive/iterative manner. Equation (3.11) assumes true data sequence $\{\cdots, \alpha_{n-2}, \alpha_{n-1}, \alpha_n\}$ is available, which is not the case in practice. As we mentioned before, the PLL is driven by the sequence of tentative decisions within the VA. These decisions become more reliable the deeper we trace back along the trellis. In view of these facts, the following PAM based timing error signal can be formulated as

$$e[n-D] = \text{Re}\left\{\dot{y}_{n-D}(\hat{\mathbf{c}}_{n-D}, \hat{\theta}_{n-L-D}, \hat{\tau}[n-D])\right\} \tag{3.14}$$

where D is the traceback depth (delay) for computing the error and $\hat{\mathbf{c}}_{n-D}$ and $\hat{\phi}_{n-L-D}$ are taken from the best survivor path history in the VA. The PAM based timing error signal in (3.14) has features in common with the one derived in [12] using the conventional CPM model in (2.1). A large D could result in longer delays in the timing recovery loop, but our observation in Chapter 6, which parallels the finding in [12], is that $D = 1$ produces satisfactory results.

Figure 3.1 shows a discrete-time implementation of the sequence detection operation in (3.4) and the TED operation in (3.14). The discrete-time received signal $r[m]$ is sampled at a rate of N samples per symbol. A sample interpolator (See Appendix B.1) is used to synchronize the received signal based on the most recent timing estimate, $\hat{\tau}[n-D]$. The synchronized samples are fed to the MF bank, the outputs of which form the values in the set $\{x_{k,n}\}_{k\in\mathcal{K}}$. The MF outputs are sampled at the symbol rate at the proper timing instant, and these MF samples are used to update the branch metrices within the VA in (3.4). In addition to the samples of $\{x_{k,n}\}_{k\in\mathcal{K}}$ that are used in the VA,

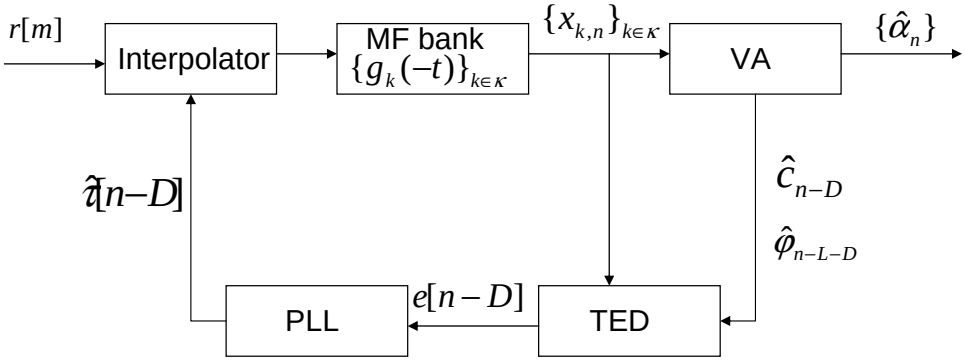

Figure 3.1. Discrete-time implementation of the PAM-based decision-directed timing recovery system for CPM.

an *early* sample of each $\{x_{k,n}\}_{k\in\mathcal{K}_{\text{TED}}}$ is taken, as well as a *late* sample. The *difference* between the early and late samples is used to approximate the *derivative* $\dot{x}_{k,n}(t)$. This procedure is detailed further in [12]. Once the error signal $e[n-D]$ is formed, it is fed to a phase-locked loop (PLL), which in turn outputs the timing estimate $\hat{\tau}[n-D]$.

3.1.3 Phase Recovery and PAM Based Phase Error Detector Implementation

The PAM based maximum likelihood phase recovery was derived in [8], assuming perfect knowledge of symbol timing. In this section we derive the same assuming that the symbol sequences are known or recovered according to 3.1.1. For the purpose of easy illustration we ignore the symbol timing and the frequency offset in (3.1), so that the signal model at the receiver becomes

$$r(t) = s(t;\boldsymbol{\alpha})e^{j\theta} + w(t). \tag{3.15}$$

The conditional likelihood formulation for a hypothesized value of $\tilde{\theta}$ can be shown as

$$\Lambda(\boldsymbol{r}|\tilde{\theta}) = \text{Re}\left\{\int_0^{L_0T_s} r(t)s^*(t;\boldsymbol{\alpha})e^{-j\tilde{\theta}}\,dt\right\}. \tag{3.16}$$

Substituting (2.7) of $s(t;\boldsymbol{\alpha})$ into (3.16) the likelihood function may be expressed as

$$\Lambda(\boldsymbol{r}|\tilde{\theta}) = \text{Re}\left\{ e^{-j\tilde{\theta}} \sum_{k=0}^{N-1} \sum_{i} b_{k,i}^{*} x_{k,i} \right\} \tag{3.17}$$

with the PED MF outputs $x_{k,i}$ defined as

$$x_{k,i} \triangleq \int_{iT_s}^{(i+D_k)T_s} r(t) g_k(t - iT_s)\, dt \tag{3.18}$$

The maximum of $\Lambda(\boldsymbol{r}|\tilde{\theta})$ is found by setting the partial derivative of (3.17) with respect to $\tilde{\theta}$ equal to zero. Thus, the phase error detector formulation can be expressed as

$$\sum_{i=0}^{L_0-1} \text{Im}\left\{ z_i(\mathbf{c}_i, \phi_{i-L}) e^{-j\tilde{\theta}} \right\} = 0 \tag{3.19}$$

where the PED increment $z_i(\mathbf{c}_i, \phi_{i-L})e^{-j\tilde{\theta}}$ is

$$z_i(\mathbf{c}_i, \phi_{i-L}) e^{-j\tilde{\theta}} = e^{-j\tilde{\theta}} \sum_{k \in \mathcal{K}_{\text{PED}}} b_{k,i}^{*} x_{k,i} \tag{3.20}$$

As before, some important observations made for (3.19) are given below:

1. From an implementaion perspective, the decision-directed phase recovery is performed by selecting the information sequence from the best survivor path of VA at each time step according to method described in Section 3.1.1, and then using those decisions to drive the PED.

2. To achieve satisfactory tracking performance, the number of PAM components can be less in PED than what is used for sequence detection. This reduces the number of filters required for PED. There is no requirement for derivative matched filters, so the same or a subset of these filters, used for sequence detec-

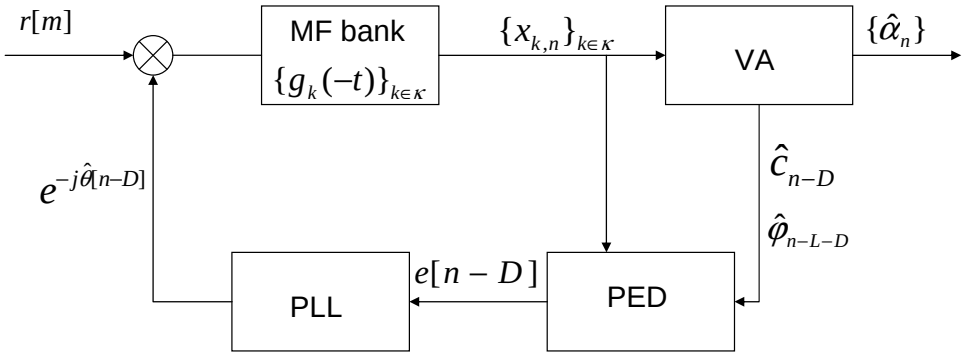

Figure 3.2. Discrete-time implementation of the PAM-based decision-directed phase recovery system for CPM.

tion purpose can be used for phase recovery.

As with the TED implementation, the maximization of (3.19) is accomplished by an iterative search through a gradient algorithm. As the formula shows, (3.11) assumes the knowledge of the true data in a data-aided environment $\{\cdots, \alpha_{n-2}, \alpha_{n-1}, \alpha_n\}$. A more practical substitute for the true data sequence is the sequence of tentative decisions within the VA, which become more reliable as we trace back along the trellis. Therefore, the formulation for the PAM based PED error can be shown as

$$e[n-D] = \text{Im}\left\{ z_{n-D}(\hat{\mathbf{c}}_{n-D}, \hat{\phi}_{n-L-D}) e^{-j\hat{\theta}[n-D]} \right\} \tag{3.21}$$

where D is the traceback depth, along the best survivor, necessary to make decisions which are reliable enough to direct the PLL. $\hat{\mathbf{c}}_{n-D}$ and $\hat{\phi}_{n-L-D}$ are taken from the path history of the best survivor in the VA.

Figure 3.2 shows a discrete-time implementation of the sequence detection operation in (3.4) and PED operation in (3.21). The discrete-time received signal $r[m]$ is sampled at a rate of N samples per symbol. Assuming the samples are time synchronized, they are fed to the MF bank, the outputs of which form the values in the set $\{x_{k,n}\}_{k\in\mathcal{K}}$. The MF outputs are sampled at the symbol rate at the perfect timing instant,

and these MF samples are used to update the branch metrics within the VA, i.e. (3.4). Once the error signal $e[n-D]$ is formed through the PED, it is fed to a phase-locked loop (PLL), consisting of a loop filter and a VCO that converts the error signal voltage to a more suitable phase estimate $\hat{\theta}[n-D]$.

3.2 Receiver without Explicit Recovery of Phase: Noncoherent Detection

When the carrier phase $\theta(t)$ is unknown but slowly varying, i.e., it can be assumed to be constant over several symbol times, then we can detect the information symbols and the symbol timing offset by noncoherent methods. In such a formulation, the phase recovery is implicit and does not require to be recovered seperately. The noncoherent approach was used in [16]. To obtain the formulation for noncoherent detection we assume the received signal has no carrier frequency offset and has the form

$$r(t) = s(t-\tau;\boldsymbol{\alpha})e^{j\theta} + w(t) \tag{3.22}$$

The metric increment for the VA in (3.5) changes to accomodate the *phase reference* as

$$y_{NC,i}(\tilde{\mathbf{c}}_i', \phi_{i-L'}, \tilde{\tau}) = Q_i^*(\tilde{S}_i) y_i(\tilde{\mathbf{c}}_i', \phi_{i-L'}, \tilde{\tau}). \tag{3.23}$$

where $Q_i^*(\cdot)$ is defined as the phase reference and can be updated after each symbol time index i via the recursion

$$Q_{i+1}(\tilde{E}_i) = aQ_i(\tilde{S}_i) + (1-a)y_i(\tilde{\mathbf{c}}_i', \tilde{\theta}_i, \tilde{\tau}). \tag{3.24}$$

where $0 \leq a < 1$ is the forgetting factor, $\tilde{S}_i$ is the starting state and $\tilde{E}_i$ is the ending state for each path in the VA. Usually, the value of a is chosen close to 1 as the BER is observed to be affected more as the value of a goes down. In our simulations, we select $a = 0.875$. In the recursion in the VA, first, the cumulative metric update using the branch metric increment (3.23) is performed after each time index to obtain the survivors at each ending state. Next, the phase reference is updated in (3.24) for each ending state $\tilde{E}_i$. Finally, the TED increment for noncoherent timing recovery is obtained by using $Q_i(\tilde{S}_i)$ and $y_i(\tilde{\mathbf{c}}_i', \tilde{\theta}_i, \tau)$ from each surviving branch at each ending state

$$\dot{y}_{NC,i}(\mathbf{c}_i', \phi_{i-L'}, \tilde{\tau}) = Q_i^*(\tilde{S}_i)\dot{y}_i(\mathbf{c}_i', \phi_{i-L'}, \tilde{\tau}). \tag{3.25}$$

3.3 Frequency Recovery and PAM Based Frequency Error Detector Implementation

We define ν as the frequency of the carrier. The maximum likelihood estimate of ν as mentioned earlier was first derived in [10]. To suit our purpose, we explain here only the important steps leading to the final expression. To do that, first, we model the received signal as in (3.1). Also, ν, θ, τ and $\boldsymbol{\alpha}$, all are taken as unknown parameters. Since this frequency recovery algorithm is NDA, it does not require knowledge of information, symbol timing and carrier phase. Using (2.7), the signal (3.1) observed at the receiver can be represented in the form

$$r(t) = e^{j(2\pi\nu t+\theta)}\sqrt{\frac{E_s}{T_s}}\sum_{k=0}^{N-1}\sum_{i} b_{k,i}g_k(t-\tau-iT_s) + w(t) \tag{3.26}$$

The log-likelihood function for the channel output observed over an interval $0 \leq t \leq L_0 T_s$ is described in [10] as a joint likelihood function that has the form

$$\Lambda(\tilde{\nu}, \tilde{\theta}, \tilde{\tau}, \tilde{\boldsymbol{\alpha}}) = \text{Re}\left\{ e^{-j\tilde{\theta}} \sum_{k=0}^{N-1} \sum_{i=0}^{L_0-1} x_k(iT_s + \tilde{\tau}) \tilde{b}_{k,i}^* \right\} \tag{3.27}$$

Where $x_k(t)$ is the response to $r(t)e^{j2\pi\tilde{\nu}t}$ of a filter matched to $g_k(t)$ and its expression can be found in [10]. So, the marginal likelihood function $\Lambda(\tilde{\nu})$ is found by averaging out the other parameters. We ignore the the intricate details of the derivation and focus on the final expression which is given as

$$\Lambda(\tilde{\nu}) = \int_0^{L_0 T_s} \left[\sum_{k=0}^{N-1} |x_k(t)|^2 \right] dt \tag{3.28}$$

To maximize $\Lambda(\tilde{\nu})$, we set the derivative of $\Lambda(\tilde{\nu})$ with respect to $\tilde{\nu}$ equal to zero and obtain the formulation for the frequency difference detector (FDD) as

$$T \sum_{l=1}^{2L_0} \sum_{k=0}^{N-1} \text{Im}\left\{ x_k\left(\frac{lT_s}{2} + t_0\right) y_k^*\left(\frac{lT_s}{2} + t_0\right) \right\} = 0 \tag{3.29}$$

where the sampling phase t_0 is chosen arbitrarily in the interval $0 \leq t \leq T_s/2$ and $y_k(t)$ is the response to $r(t)e^{-j2\pi\tilde{\nu}t}$ of a filter matched to $\dot{g}_k(-t)$ and has a lengthy expression defined in [10].

The solution to (3.29) is carried out by an iterative search to find a value $\tilde{\nu}$ as follows: first, we collect both $(n+1)$-th and n-th terms into the error $e[n]$ so that, $\tilde{\nu}(n)$ can be updated every T_s seconds instead of $T_s/2$. Second, the number of matched filters N is limited to a value $|\mathcal{K}_{\text{FDD}}| \leq N$ to reduce the computing load as much as possible.

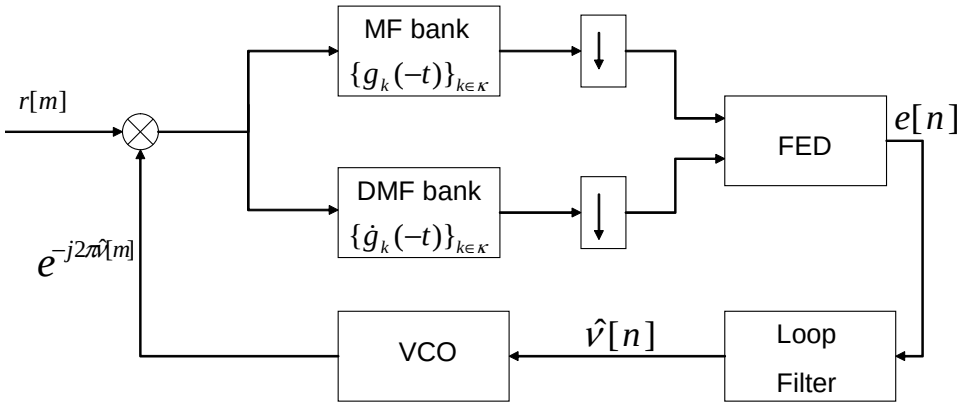

Figure 3.3. Discrete-time implementation of the PAM-based non-data-aided frequency recovery system for CPM.

Considering these factors, we can summarize the error function as

$$\begin{aligned} e[n] = \Gamma \sum_{k\in\mathcal{K}_{\text{FDD}}} \text{Im}\{&x_k(nT_s - T_s/2 + t_0)y_k^*(nT_s - T_s/2 + t_0) \\ &+ x_k(nT_s + t_0)y_k^*(nT_s + t_0)\} \end{aligned} \tag{3.30}$$

where Γ is a normalizing constant, and its value is given as $\Gamma \triangleq E_s T_s^2/4$.

Figure 3.3 shows a discrete-time implementation of the FDD operation in (3.30). Here, the blocks labeled MF and DMF represent matched filter and derivative matched filter, respectively. The received waveform is first fed to an anti-aliasing filter (not shown in the figure) and then sampled at a rate $1/T \triangleq N/T_s$. The samples $r[m]$ (where $m \triangleq nT$) are counter-rotated by $2\pi\hat{\nu}[m]$ and are fed to the MF and DMF. Filter outputs are decimated to $1/T_s$ before entering the error generator. The loop filter performs the digital integration on the error and an estimate of $\tilde{\nu}[n]$ is generated. The VCO generates the sequence $e^{-j2\pi\hat{\nu}[m]}$ according to the method given in Appendix B.2. It is seen, however, from simulation results that only one pair of MF and DMF is sufficient to produce satisfactory result. This also reduces the computation load on the detector.

Chapter 4

Performance Analysis and Bounds for Tracking Error Variances

In this chapter, we briefly discuss several performance lower bounds, analyze several criteria for the PLL considerations, and develop S-curves that play important roles in determining signal acquisition and tracking behavior of the error detectors. All the formulations we discuss here already exist in the literature. We find it relevant to spare a chapter for this because we use these to evaluate the performance of the proposed *joint* carrier frequeny, symbol timing and carrier phase synchronizers discussed later.

4.1 Modified Cramer-Rao Bound for CPM

We use the modified Cramer-Rao bound (MCRB) [19] to establish a lower bound on the degree of accuracy to which τ, θ and ν can be estimated. To find the MCRB for timing, We follow the approach in [20, Ch. 2] and take the complex-baseband signal

model with channel delay τ, carrier/channel phase θ and carrier frequency ν as

$$s(t;\boldsymbol{\alpha},\tau,\theta,\nu)=\sqrt{\frac{E_s}{T_s}}\exp\left\{j2\pi h\sum_i \alpha_i q(t-\tau-iT_s)\right\}\exp\left\{j2\pi\nu t+j\theta\right\}. \quad (4.1)$$

The MCRB with respect to τ for a baseband signal is defined as [20]

$$\text{MCRB}(\tau)\triangleq\frac{N_0/2}{\text{E}_{\boldsymbol{u_\tau}}\left\{\int_0^{T_0}\left|\frac{\partial s(t;\tau,\boldsymbol{u_\tau})}{\partial\tau}\right|^2 dt\right\}}$$

where $\boldsymbol{u_\tau}=\{\boldsymbol{\alpha},\theta,\nu\}$ contains all the unwanted parameters that need to be averaged out. $T_0\triangleq L_0T_s$ is the length of the observation interval and assume that L_0 is an integer. After taking the partial derivative with respect to τ of (4.1), we obtain the following integral

$$T_sh^2\int_0^{T_0}\sum_i f^2(t-\tau-iT_s).$$

The expression for the energy of the frequency pulse over the total pulse length in time L_0T_s can be computed as

$$C_f\triangleq T_s\int_0^{LT_s} f^2(t)dt \quad (4.2)$$

The final expression for the MCRB (normalized to the symbol rate) is

$$\frac{1}{T_s^2}\times\text{MCRB}(\tau)=\frac{1}{8\pi^2h^2C_\alpha C_fL_0}\times\frac{1}{E_s/N_0} \quad (4.3)$$

where $C_\alpha\triangleq\text{E}\{\alpha_n^2\}=(M^2-1)/3$ for uncorrelated M-ary data symbols. The observation inteval L_0 is related to the equivalent normalized noise bandwidth as $B_\tau T_s=1/2L_0$. For the special case of LREC we have $C_f=C_{L\text{REC}}\triangleq 1/(4L)$, and for the special case of LRC we have $C_f=C_{L\text{RC}}\triangleq 3/(8L)$. For all other frequency pulse shapes, (4.2) can be computed analytically or numerically. In Chapter 6, we use the

MCRB(τ) to evaluate computer simulation results for the *normalized timing error variance*, which is defined as

$$\frac{1}{T_s^2} \times \sigma_\tau^2 \triangleq \frac{1}{T_s^2} \times \text{Var}\left\{\hat{\tau}[n] - \tau\right\}. \tag{4.4}$$

The MCRB with respect to θ for a baseband signal is defined in [20] as

$$\text{MCRB}(\theta) \triangleq \frac{N_0/2}{\text{E}_{\boldsymbol{u_\theta}}\left\{\int_0^{T_0} \left|\frac{\partial s(t;\theta,\boldsymbol{u_\theta})}{\partial\theta}\right|^2 dt\right\}}. \tag{4.5}$$

where $\boldsymbol{u_\theta} = \{\boldsymbol{\alpha}, \tau, \nu\}$ contains all the unwanted parameters that need to be averaged out. After going through the derivation using (4.1) as the signal model the expression for the denominator yields

$$\text{E}_{\boldsymbol{u_\theta}}\left\{\int_0^{T_0} \left|\frac{\partial s(t;\theta,\boldsymbol{u_\theta})}{\partial\theta}\right|^2 dt\right\} = E_s L_0. \tag{4.6}$$

Inserting (4.6) into (4.5) The final expression for MCRB for θ can be expressed as

$$\text{MCRB}(\theta) = \frac{1}{2L_0} \times \frac{1}{E_s/N_0} \tag{4.7}$$

where the observation inteval L_0 is related to the equivalent normalized noise bandwidth as $B_\theta T_s = 1/2L_0$. We use the MCRB(θ) to evaluate computer simulation results for the *phase error variance*, which is defined as

$$\sigma_\theta^2 \triangleq \text{Var}\left\{\hat{\theta}[n] - \theta\right\}. \tag{4.8}$$

The MCRB with respect to ν for a baseband signal is defined in [20] as

$$\text{MCRB}(\nu) \triangleq \frac{N_0/2}{\text{E}_{\boldsymbol{u_\nu}}\left\{\int_0^{T_0}\left|\frac{\partial s(t;\nu,\boldsymbol{u_\nu})}{\partial \nu}\right|^2 dt\right\}} \tag{4.9}$$

where the expectation is taken over $\boldsymbol{u_\nu} = \{\boldsymbol{\alpha}, \tau, \theta\}$ that contains all the unwanted parameters. After going through the derivation using (4.1) as the signal model the expression for the denominator yields

$$\text{E}_{\boldsymbol{u_\nu}}\left\{\int_0^{T_0}\left|\frac{\partial s(t;\nu,\boldsymbol{u_\nu})}{\partial \nu}\right|^2 dt\right\} = \frac{3T_s}{8\pi^2 E_s L_0^3 T_s^3}. \tag{4.10}$$

Inserting (4.10) into (4.9) yields the final expression for MCRB for ν in terms of the equivalent noise bandwidth $B_\nu T_s = 1/2L_0$ as

$$T_s^2 \times \text{MCRB}(\nu) = \frac{3}{2\pi^2 L_0^3} \times \frac{1}{E_s/N_0}. \tag{4.11}$$

We use the MCRB(ν) to evaluate computer simulation results for the *normalized frequency error variance*, which is defined as

$$T_s^2 \times \sigma_\nu^2 \triangleq T_s^2 \times \text{Var}\left\{\hat{\nu}[n] - \nu\right\}. \tag{4.12}$$

4.2 PLL Considerations

The PLL is an essential part of each of the error detectors we discussed so far. The performance of the PLL depends on the loop filter bandwidth, normalized with respect to the symbol rate, which controls the step size by which it increments or decrements the error in order to lock on to the correct value. During lock acquisition, the loop band-

width of the PLL is set relatively high and while tracking, it is set to a lower value. PLLs can have several orders. A first-order PLL is easy to implement but performs worse under frequency offsets than a seccond-order PLL. We use the relationship between the observation length L_0 of a feedforward scheme and the *normalized loop bandwidth* BT_s of a feedback scheme, $L_0 = \frac{1}{2BT_s}$, to explain the PLL workings. However, this relationship is valid for only a first-order PLL [12].

4.2.1 PLL for TED

We use a standard first-order PLL implementation for timing recovery; the raw TED output $e_\tau[n]$ is refined into a more suitable timing estimate $\hat{\tau}[n]$ via the update $\hat{\tau}[n] \triangleq \hat{\tau}[n-1] + \gamma_\tau e_\tau[n]$. This process is recursive and is performed after every symbol index n. $\gamma_\tau \triangleq \frac{4B_\tau T_s}{k_{p\tau}}$ is called the PLL *step size*. $k_{p\tau}$ is the positive slope of the *S-curve* characteristic of the TED at its zero crossing points and is explained in Section 4.3.1.

4.2.2 PLL for PED

In all the simulations for carrier phase recovery, we have used first and second order PLL for PEDs depending on the presence of carrier frequency offset in the received signal. First-order PLLs can be used in the presence of very little ($10^{-4}T_s$) or no frequency offset. When implemented, a standard first-order PLL converts the raw PED output $e_\theta[n]$ into a phase estimate $\hat{\theta}[n]$ through the update $\hat{\theta}[n] \triangleq \hat{\theta}[n-1] + \gamma_\theta e_\theta[n]$ which is performed after each symbol index n. The *step size* for phase PLL is $\gamma_\theta \triangleq \frac{4B_\theta T_s}{k_{p\theta}}$ where the constant $k_{p\theta}$ is obtained from the *S-curve* characteristic of the PED as per Section 4.3.2. The second-order PLL is used when there is a relatively large amount of phase jitter caused by the Doppler shift or local osclillator instabilities resulting in

a carrier frequency shift in the system, and, can be implemented as methods described in [18]. Thus, the new phase estimate is obtained as $\hat{\theta}[n] \triangleq \hat{\theta}[n-1]+\gamma_\theta \xi[n]$ where $\xi[n]$ is the update from the first order loop filter obtained from the phase error $e_\theta[n]$ as $\xi[n] = \xi[n-1]+(K1+K2)k_{p\theta}e_\theta[n]-K2k_{p\theta}e_\theta[n-1]$. Here, $K1$ and $K2$ are the proportional and integration constants repectively and their values can be found out from [18, p.738, Equation C.61], with the damping coefficient as $\zeta = \frac{1}{\sqrt{2}}$. Interesting to note here is that the relationship between the observation length L_0 and the *normalized loop bandwidth* $B_\theta T_s$ is not valid in this case and the tracking accuracy has to be evaluated based on the BER instead of MCRB(θ).

4.2.3 PLL for FDD

In this case, a first-order PLL refines the raw FDD output $e_\nu[n]$ into a more suitable frequency estimate $\hat{\nu}[n]$ via the update $\hat{\nu}[n] \triangleq \hat{\nu}[n-1]+\gamma_\nu e_\nu[n]$, performed after each symbol index n. The PLL *step size* is $\gamma_\nu \triangleq \frac{4B_\nu T_s}{k_{p\nu}}$ where the constant $k_{p\nu}$ is obtained from the *S-curve* characteristic of the FDD.

4.3 S-Curves

S-curves are useful for characterizing the behavior of the error detectors. They are defined as the *expected value* of the error detector output as a function of the respective offsets (timing, phase and frequency). S-Curve charaterization of a system is two fold. First, it gives a method of identifying the stable lock points which are the zero-crossing positive slope points on the curve. These determine if any false lock points exist. Second, the S-curve also determines the value of k_p, mentioned in Section 4.2, as the slope of the S-curve evaluated at an offset $\delta = 0$. This in turn, is used to determine the step size for the PLL. In the following subsections we define the S-curve of each error

detector. The analytical expressions for S-curves of the TED and the PED, assuming known symbol sequences are briefly described in Appendix A. In the practical case of decision-directed recovery for symbol timing and carrier phase, where the known symbols in the data-aided case are replaced by the decisions taken from the VA, S-curves for M-ary partial-response CPMs show false lock points. However, the NDA S-curve of FDD ensures that there is no false lock.

4.3.1 S-Curve for TED

The formulation for S-curve for TED as per the definition given above can be obtained as

$$S(\delta_\tau) \triangleq \sqrt{E_s/T_s} \cdot \mathrm{E}\big\{e_\tau[n] \,|\, \delta_\tau\big\}, \tag{4.13}$$

where the timing offset is defined as $\delta_\tau \triangleq \tau - \hat{\tau}$. $e_\tau[n]$ is the error output of the TED after every symbol index n.

4.3.2 S-Curve for PED

The S-curve for PED is defined as the *expected value* of the PED output $e_\theta[n]$ as a function of the *phase offset*, i.e.

$$S(\delta_\theta) \triangleq \sqrt{E_s/T_s} \cdot \mathrm{E}\big\{e_\theta[n] \,|\, \delta_\theta\big\}, \tag{4.14}$$

where the phase offset is defined as $\delta_\theta \triangleq \theta - \hat{\theta}$.

4.3.3 S-Curve for FDD

The frequency S-curve is defined as the *expected value* of the FDD output $e_\nu[n]$ as a function of the *normalized frequency offset*, i.e.

$$S(\delta_\nu) \triangleq \sqrt{E_s/T_s} \cdot \mathrm{E}\big\{e_\nu[n] \,|\, \delta_\nu\big\}, \tag{4.15}$$

where the normalized frequency offset is defined as $\delta_\nu \triangleq \nu - \hat{\nu}$.

Chapter 5

PAM Receivers with *Joint* Synchronization

Up to this point, we have knowledge about how the frequency, phase and timing recovery are done separately for a CPM signal using its PAM representations. In this chapter, we first describe a *joint* carrier phase and symbol timing recovery for PAM based CPM receivers algorithm that may be employed with any CPM format, and with either full or reduced state detectors. We aim to find an optimal solution in terms of complexity reduction and error tracking performance. Their implementations, as discussed in previous chapters, are fully digital and have excellent tracking performance. Later, we look into the same algorithms but in the presence of a large frequency offset (on the order of the symbol rate). In particular, we describe a *joint* frequency, phase and timing recovery method for PAM based CPM receivers. This is another major contribution of this thesis as shown in Figure 1.1.

In Chapter 6, we present the performance of these algorithms we discussed in this chapter with examples. Finally, we revisit the problem of false lock for M-ary partial-response systems in Chapter 7 where we propose a novel solution to the false lock

problem in connection with the PAM based receivers algorithms we describe in this chapter.

5.1 Joint Timing and Phase Recovery

We explored the so-called decision-directed (DD) methods of symbol timing and carrier phase recovery in Chapter 3. In this section, first, we simply simultaneously run these two algorithms to form a *joint* timing and phase recovery technique for PAM-based CPM receivers assuming zero frequency offset in the carrier. To do that, we consider the signal model presented in (3.1) and set the frequency offset $\nu = 0$. The phase and timing loop are operated separately, with the decision for the symbol directed recovery taken from the best survivor of the Viterbi decoder. Therefore, for the received signal with unknown symbol timing offset τ and carrier phase offset θ,

$$r(t) = s(t - \tau; \boldsymbol{\alpha})e^{j\theta} + w(t) \tag{5.1}$$

The TED formulation in 3.11 and the PED formulation in 3.19 will now change to solve the following equations

$$\sum_{i=0}^{L_0-1} \text{Re}\left\{\dot{y}_i(\mathbf{c}_i, \phi_{i-L}, \tilde{\tau})e^{-j\tilde{\theta}}\right\} = 0 \tag{5.2}$$

and

$$\sum_{i=0}^{L_0-1} \text{Im}\left\{z_i(\mathbf{c}_i, \phi_{i-L}, \tilde{\tau})e^{-j\tilde{\theta}}\right\} = 0 \tag{5.3}$$

respectively.

The following points are of importance:

1. There are assumed to be no interactions between timing and phase locked loops.

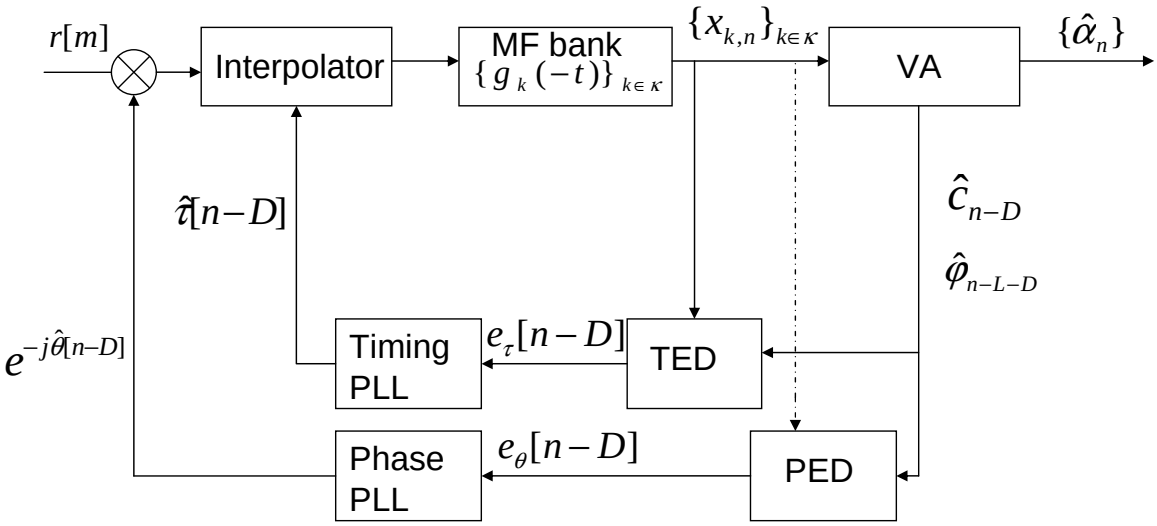

Figure 5.1. Discrete-time implementation of PAM based joint timing and phase recovery.

In other words, they are operated independently.

2. The number of matched filters may vary for TED and PED. Each one is also independent of the matched filters employed for sequence detection. Conventionally, more MFs are used for sequence detection in order to obtain reliable decisions from the VA.

Figure 5.1 shows the digital implementation of the PAM receiver with *joint* timing and phase recovery. The incoming waveform is passed through an antialiasing filter with a bandwidth large enough not to introduce distortion in the signal. The discrete-time output of the filter is then sampled at a rate of N samples per symbol. They are then fed to a sample interpolator used to time-align the received signal. The timing estimate is obtained from the TED error after every symbol time according to $\hat{\tau}[n] \triangleq \hat{\tau}[n-1] + \gamma_\tau e_\tau[n-D]$ with

$$e_\tau[n-D] = \text{Re}\left\{\dot{y}_{n-D}(\hat{\mathbf{c}}_{n-D}, \hat{\phi}_{n-L-D}, \hat{\tau}[n-D])e^{-j\hat{\theta}[n-D]}\right\} \tag{5.4}$$

The synchronized samples are also used to obtain the PED error according to (5.3). The error obtained is used to drive the phase PLL, consisting of a loop filter and a VCO, converting the phase error signal voltage to a suitable phase estimate according to $\hat{\theta}[n] \triangleq \hat{\theta}[n-1] + \gamma_\theta e_\theta[n]$ with

$$e_\theta[n-D] = \text{Im}\left\{ z_{n-D}(\hat{\mathbf{c}}_{n-D}, \hat{\phi}_{n-L-D}, \hat{\tau}[n-D]) e^{-j\hat{\theta}[n-D]} \right\} \tag{5.5}$$

The D is the delay parameter in the error signal, conveniently chosen as 1.

The PLL step sizes $\gamma_\tau \triangleq \frac{4B_\tau T_s}{k_{p\tau}}$ and $\gamma_\theta \triangleq \frac{4BT_s}{k_{p\theta}}$ can be found from the corresponding loop filter bandwidths of timing and phase PLL. $k_{p\tau}$ and $k_{p\theta}$ are the slopes at the zero-crossings of the timing and phase S-curves respectively.

A comparative study of coherent and noncoherent *joint* timing and phase recovery algorithms for conventional and various suboptimal PAM receivers is presented in Chapter 6 for binary and M-ary CPM schemes.

5.2 *Joint* Frequency, Timing and Phase Recovery

So far, we have not considered the effects due to oscillator instabilities and the Doppler effect. These introduce frequency distortion in the signal which can be as large as the symbol rate. We employ the existing PAM based non data aided (NDA) frequency detection algorithm discussed in Section 3.3 first to find an estimate $\tilde{\nu}$ of the frequency offset in the received signal. We used this frequency offset to counter-rotate the received waveform at an angular frequency of $2\pi\tilde{\nu}$ before feeding the signal for timing and phase recovery as already explained in Section 5.1. In our discussion here, we distinguish between two major cases:

1. The frequency offset is much smaller than $1/T_s$ that occurs when a receiver is

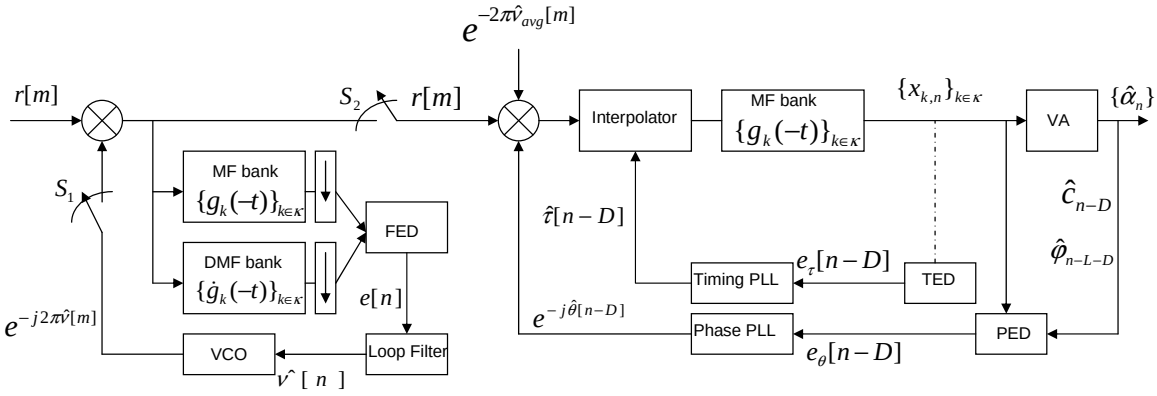

Figure 5.2. Discrete-time implementation of PAM based joint frequency, timing and phase recovery.

operating in steady-state conditions. In this case, a *joint* timing and frequency recovery is possible, in which, the timing recovery is done at first and then exploited for estimating $\tilde{\nu}$ [14].

2. The frequency offset is on the order of the symbol rate $1/T_s$. This occurs during initial acquisition in low-capacity digital radios, aeronautical telemetry and satellite communication systems. In these applications, it can be reasonably assumed that the data symbols, the carrier phase, and the timing information all are unknown. Therefore, reducing the frequency error to a small percentage of the symbol rate is always recommended before attempting to begin other synchronizations.

Figure 5.2 shows the digital implementation of the PAM receiver with *joint* frequency, timing and phase recovery. We base our approach considering both coherent and noncoherent cases discussed above in that we apply the NDA frequency recovery algorithm discussed in Section 3.3 to the incoming signal to obtain a final estimate $\tilde{\nu}$ by averaging $\tilde{\nu}$ over a number of preamble symbols whose lengths can be determined by simulations for different CPM modulation formats. While estimating the frequency, S_1

remains closed and S_2 opened. Once the average estimate $\tilde{\nu}_{avg}$ is done the FDD loop is disconnected by opening S_2. This estimate $\tilde{\nu}_{avg}$ is then used to counter-rotate the received signal by $2\pi\tilde{\nu}_{avg}[m]$ and fed to the *joint* timing and phase detector by closing S_2. The timing and phase estimates are then obtained according to the method described in Section 5.1. We observed that accurate timing information can be obtained even in the presence of a moderate frequency offset (10% to 20% of the symbol rate). This is not the case with phase recovery. Therefore, we feed the signal output from the FDD block to noncoherent PAM based timing recovery detection discussed in Section 3.2, thus, avoiding the carrier phase recovery. A good reason for choosing the NDA frequency recovery algorithm is that it has a relatively large lock acquisition range on the order of the symbol rate depending on the variations in CPM modulation. However, we observe the performance of both coherent and noncoherent detectors under Case 2 and noncoherent CPM/PAM detectors seem to perform much better than their coherent counterparts. From the implementation perspective, the maximum likelihood based FDD described in Section 3.3 is used and the error signal is obtained as in (3.30). The raw FDD output $e_\nu[n]$ is refined into a suitable frequency estimate $\hat{\nu}[n]$ via the update $\hat{\nu}[n] \triangleq \hat{\nu}[n-1] + \gamma_\nu e_\nu[n]$ which is performed after each symbol index n. The PLL *step size* is $\gamma_\nu \triangleq \frac{4B_\nu T_s}{k_{p\nu}}$ where the constant $k_{p\nu}$ is obtained from the *S-curve* characteristic of the FDD.

A comparative study of coherent and noncoherent joint frequency, timing and phase recovery algorithms for conventional and various suboptimal PAM receivers is presented in Chapter 6 for binary and M-ary CPM schemes.

Chapter 6

Simulation Results

In this chapter, we present the tracking and BER performances of CPM schemes and their PAM based counterparts under steady-state condition over the AWGN channel. In order to compare and contrast the performance differences between the systems described here, we do the following:

- Compare the performance variations of binary and M-ary CPM.
- Study the effects of coherent and noncoherent detection of CPM.
- Observe the important results and provide recommendations to suitably replace conventional CPM systems with reduced-complexity PAM based systems.

6.1 *Joint* Timing and Phase Recovery Performance of PAM Based Receivers Under No Carrier Frequency Offsets

We now present a comprehensive comparative study of the *joint* timing and phase recovery of the existing conventional CPM receivers and our proposed PAM based receivers of binary and M-ary CPM systems. We assume that there is no extra "jitter" present because of the Doppler shift in the channel or the oscillator instabilities between

transmitter and receiver.

6.1.1 Binary GMSK: $M = 2$, $L = 4$, $h = 1/2$

We first discuss the binary GMSK scheme with $M = 2$, $L = 4$, $h = 1/2$ and $B = 1/4$, which is popularly known as "Gaussian MSK" and is the modulation scheme used for the seccond generation mobile (GSM) system, first introduced in Europe. The optimal PAM based detector for this scheme has a 16-state trellis and a bank of 8 MFs/pulses. There are a number of reduced-complexity PAM based detector configurations that are possible based on the number of PAM pulses we choose (See Appendix C.1). We select a 4-state coherent detector with $L' = 2$ that uses a bank of $|\mathcal{K}| = |\mathcal{K}_{\text{TED}}| = |\mathcal{K}_{\text{PED}}| = 2$ MFs/pulses and also works for $|\mathcal{K}_{\text{TED}}| = |\mathcal{K}_{\text{PED}}| = 1$ pulse. We then compare its detection and tracking efficiencies to that of the conventional CPM scheme. We also use noncoherent detectors with similar configurations for conventional and PAM based CPMs for comparison. In this example, and in all the subsequent examples in this chapter, we select the tentative decision delay D as 1.

Figure 6.1 and Figure 6.2 show S-curves for PAM-TED and PAM-PED for this detector obtained by computer simulations. Analytical expressions of the S-curves are also given in (A.1) and (A.4). The S-curves are shown properly marked on the figure for various PAM pulses. The curves indicate that the TED and the PED lock onto the correct timing and phasing instants at $\delta_\tau = 0$ and at $\delta_\theta = 0$ respectively. The results from computer simulations for the *decision-directed* case also conform with the corresponding analytical (data-aided) expressions. In practice, however, the *decision-directed* case is the intended implementation. Both analytical and decision-directed S-curves match near the zero-crossings as shown in the figures. We note that the decision-directed S-curve for the TED is periodic with the period T_s, and therefore, has stable

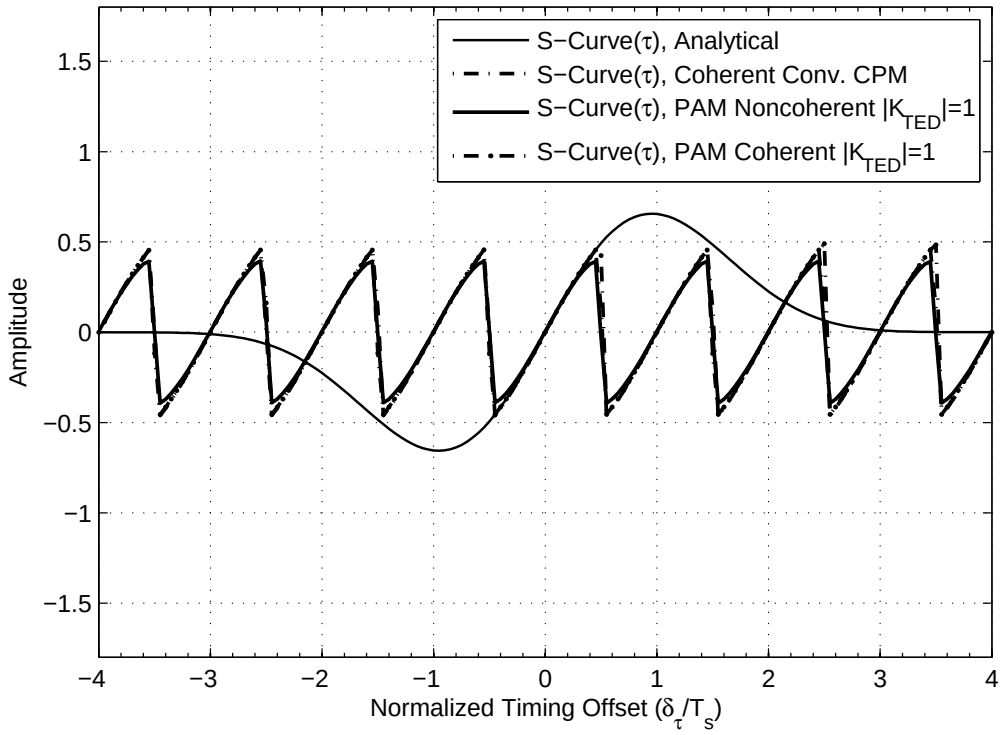

Figure 6.1. S-Curves for the TED. The modulation scheme is GMSK ($M = 2$, $L = 4$, $h = 1/2$ and $B = 1/4$).

lock points when δ_τ equals an integer multiple of T_s. For the PED, the stable lock points are the evenly distributed 4 points along a unit circle and with a period $\frac{\pi}{2}$. The performance of the decision-directed TED breaks down as δ_τ approaches half-integer multiples of T_s or δ_θ approaches half-distance on the circle between two consecutive phase lock points, due to unreliable tentative decisions within the VA.

In Figure 6.3, we compare the *normalized timing error variance* of the TED for the conventional CPM and the PAM based implementations. We also compare cases with 2 pulses and 1 pulse in the PAM based TED for coherent and noncoherent detections. The coherent TEDs show better tracking accuracy compared to the noncoherent TEDs in the fact that they operate very close to the practical lower bound of MCRB(τ). We also observe that the tracking accuracy of the reduced-complexity PAM-TEDs are very

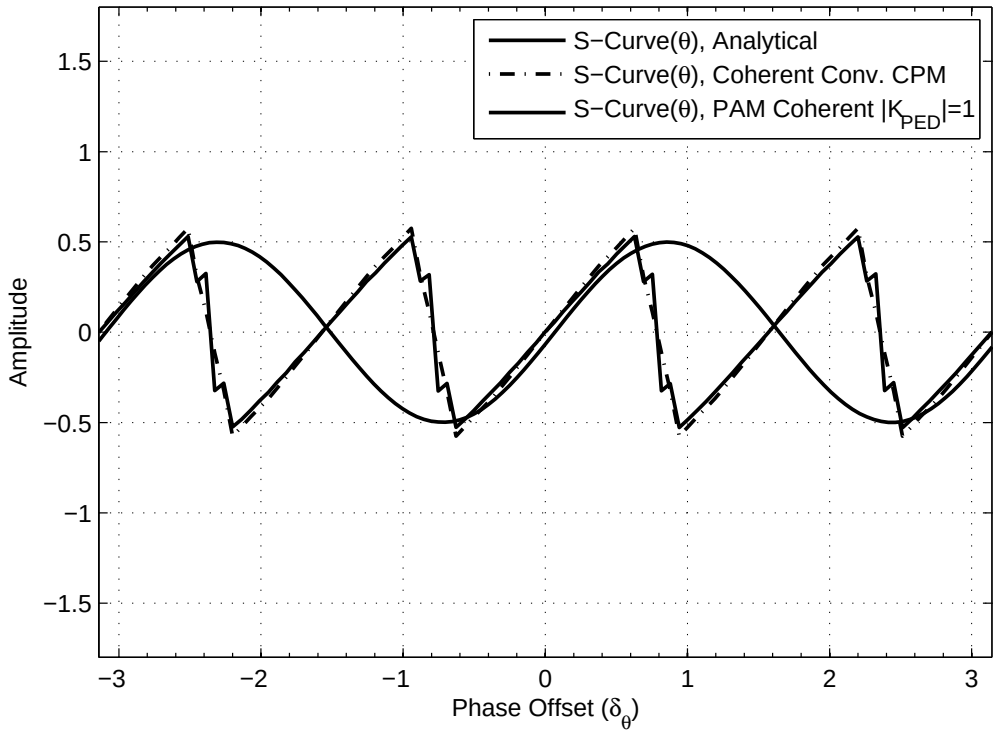

Figure 6.2. S-Curves for the PED. The modulation scheme is GMSK ($M = 2$, $L = 4$, $h = 1/2$ and $B = 1/4$).

much comparable to the original implementation of the conventional TED. Also, the performance of all the reduced-complexity configurations is quite good for small values of E_s/N_0 but at large values of E_s/N_0 it appears to deviate from the MCRB(τ) which is due to the internal noise generated by the DD algorithm. In the example considered, the relative ranking between the reduced-complexity TED configurations often fluctuates depending on the operating range of E_s/N_0 although, for the most part, the TED with 2 pulses offer better tracking performance than the TED with 1 pulse.

Next, in Figure 6.4, we compare the *phase error variance* of the PED for conventional CPM and the PAM based implementations. Like with the TED, we also consider cases with 2 pulses and 1 pulse in the PAM based PEDs for comparisons. We observe that, for lower values of E_s/N_0, the tracking performance of the reduced-complexity

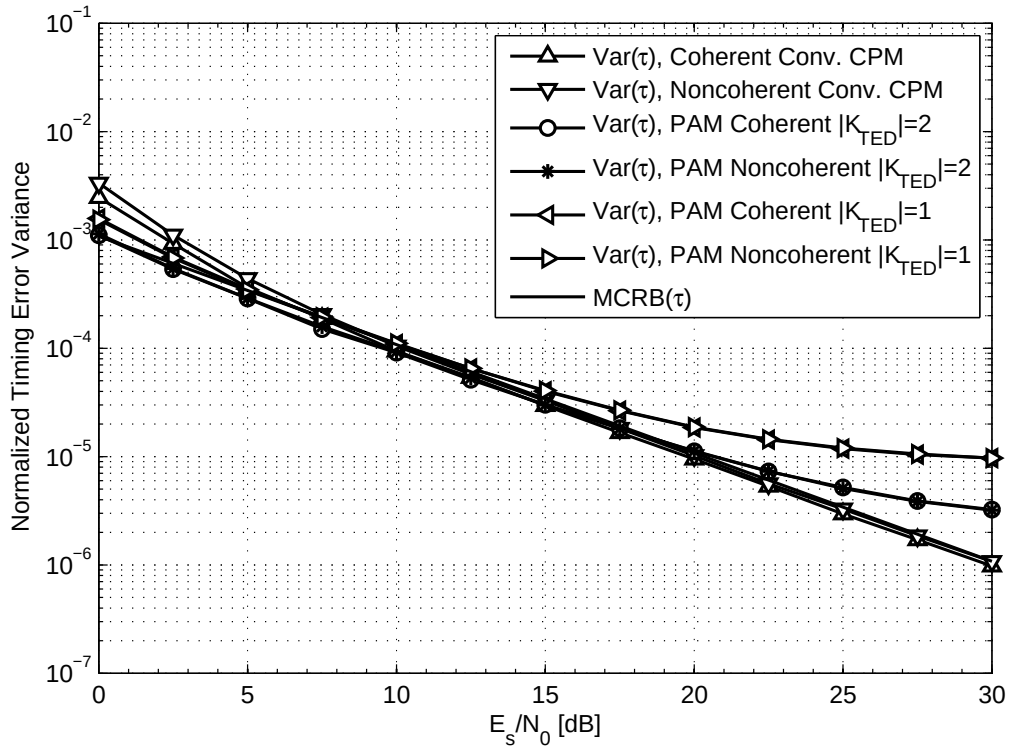

Figure 6.3. MCRB vs. normalized timing error variances for the TED. The modulation scheme is GMSK ($M = 2$, $L = 4$, $h = 1/2$, $B = 1/4$) with $B_\tau T_s = 1 \times 10^{-3}$.

PEDs are comparable to the conventional CPM PED. At relatively higher values of E_s/N_0, however, it deviates further away from the MCRB(θ) due to the internal noise generated by the DD algorithm. Here, we use only a first-order PLL for phase acquisition and tracking. In this example, both the reduced-complexity PED configurations offer similar tracking performance over the operating range of E_s/N_0.

Lastly, in Figure 6.5, we compare the BER for the conventional CPM and the PAM based configurations. The coherent conventional CPM receiver has the lowest BER and is the same as the theoretical BER for this scheme for AWGN channel. The conventional noncoherent CPM receiver is the next best: operating only about 0.2 dB off the coherent receiver at a probability of error of 10^{-4}. Reduced-complexity PAM based

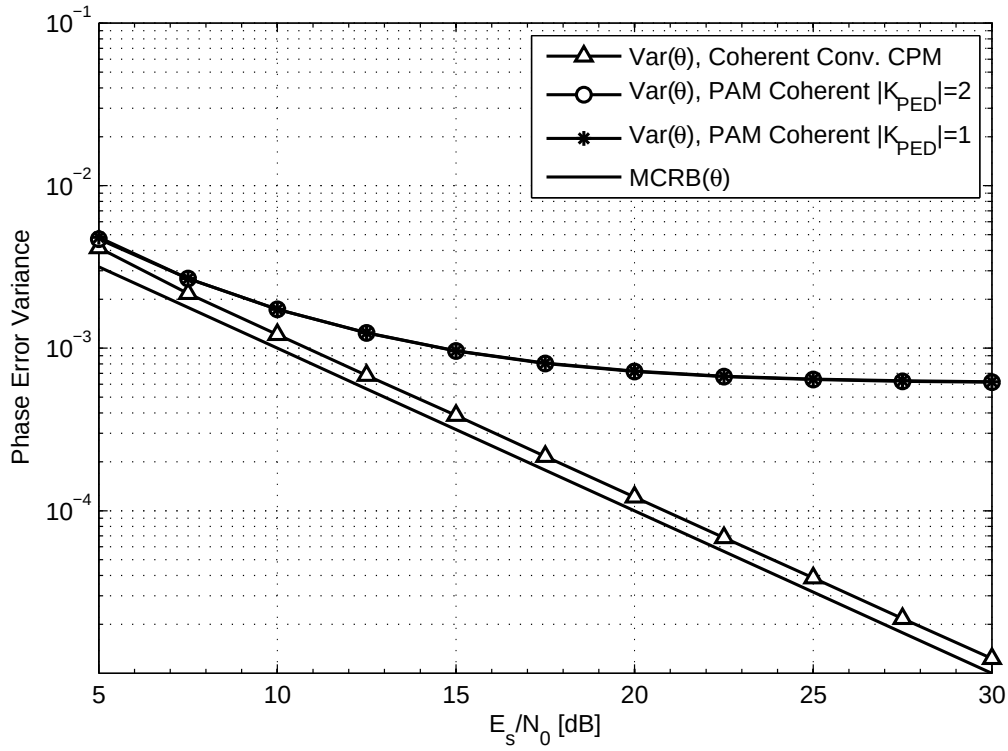

Figure 6.4. MCRB vs. phase error variances for the PED. The modulation scheme is GMSK ($M = 2$, $L = 4$, $h = 1/2$, $B = 1/4$) with $B_\theta T_s = 1 \times 10^{-2}$.

coherent receivers with $|\mathcal{K}| = |\mathcal{K}_{\text{TED}}| = 2$ MFs/pulses show good BER and within 0.5 dB of the theoretical value at a given probability of error, but with $|\mathcal{K}_{\text{TED}}| = 1$ pulse, we obtain about a 2 dB worse performance in BER. This is due to rapid deterioration of the timing tracking efficiency with $|\mathcal{K}_{\text{TED}}| = 1$, especially for higher E_s/N_0.

6.1.2 M-ary CPM: $M = 4$, $h = 1/4$, 2RC

In our seccond example, we discuss the quaternary CPM scheme with $M = 4$, $h = 1/4$ and 2RC. The optimal PAM based detector for this scheme requires a 16-state trellis and a bank of 12 MFs/pulses. Out of a number of reduced-complexity PAM based detector configurations that could be chosen (See Appendix C.2), we select a

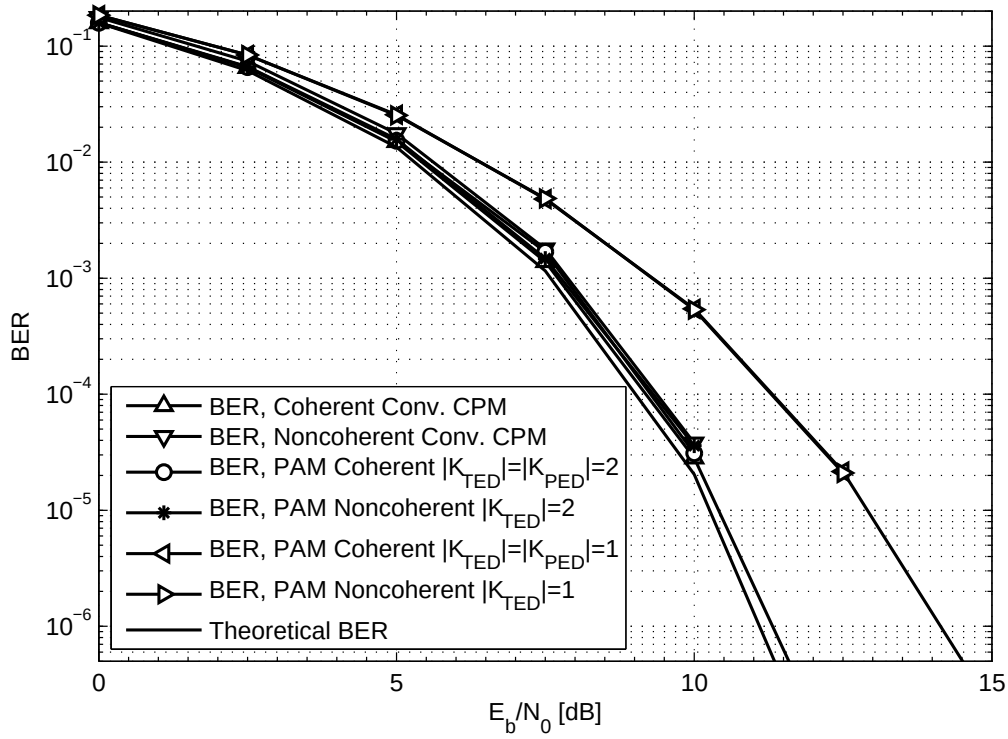

Figure 6.5. Theoretical BER vs. BER obtained for various conventional and PAM based implementaions of the GMSK modulation scheme ($M = 2$, $L = 4$, $h = 1/2$, $B = 1/4$) with $B_\tau T_s = 1 \times 10^{-3}$ and $B_\theta T_s = 1 \times 10^{-2}$.

4-state coherent detector with $L' = 1$ that uses a bank of $|\mathcal{K}| = |\mathcal{K}_{\text{TED}}| = |\mathcal{K}_{\text{PED}}| = 2$ MFs/pulses and, also, can be made to work for $|\mathcal{K}_{\text{TED}}| = |\mathcal{K}_{\text{PED}}| = 1$ pulse. We then compare their detection and tracking efficiencies to that of the conventional CPM scheme. Also, noncoherent detectors are considered for comparison.

Figure 6.6 and Figure 6.7 show S-curves for PAM-TED and PAM-PED respectively for this detector obtained from computer simulations. In this case, the second and third PAM pulses for this CPM scheme have relatively large amplitudes as seen in Figure C.2; their absence with $|\mathcal{K}_{\text{TED}}| = 1$ has resulted in lowering the amplitude of the S-curve for the TED. The curves indicate that the TED and the PED lock onto the correct timing and phasing instants at $\delta_\tau = 0$ and $\delta_\theta = 0$ respectively. We note that the decision-directed

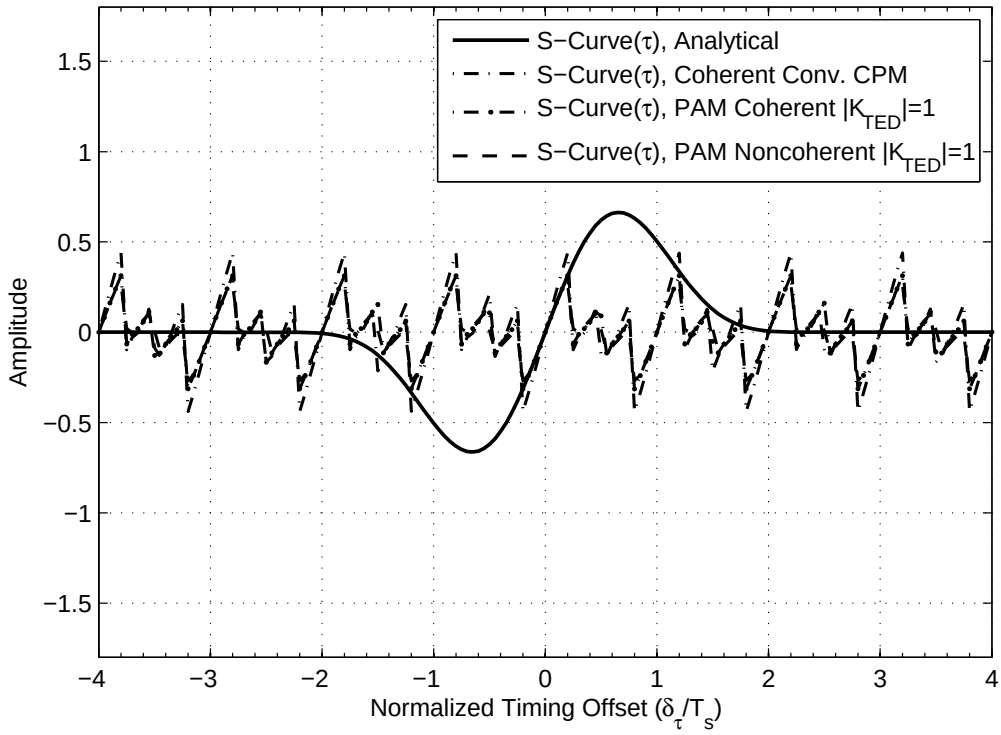

Figure 6.6. S-Curves for the TED. The modulation scheme is Quaternary CPM ($M = 4$, $L = 2$, $h = 1/4$).

S-curves for the TEDs are periodic with the period T_s, and therefore have stable lock points when δ_τ equals an integer multiple of T_s. For the PEDs, the stable lock points are the evenly distributed 8 points along a unit circle and with a period $\frac{\pi}{4}$. The simulated S-curves show that the performance of the decision-directed TED breaks down as δ_τ approaches $\frac{1}{3}T_s$. The breakdown causes additional zero crossing points with positive slope at $\frac{1}{3}T_s$ and $\frac{2}{3}T_s$. These additional points are false lock points. This is in contrast with the binary GMSK scheme discussed earlier where no such unintended lock point is created. Therefore, M-ary partial response CPM systems suffer from the problem of false lock.

In Figure 6.8, we first compare the normalized timing error variance of the TED for conventional CPM and the PAM based implementations. Cases with 2 pulses and

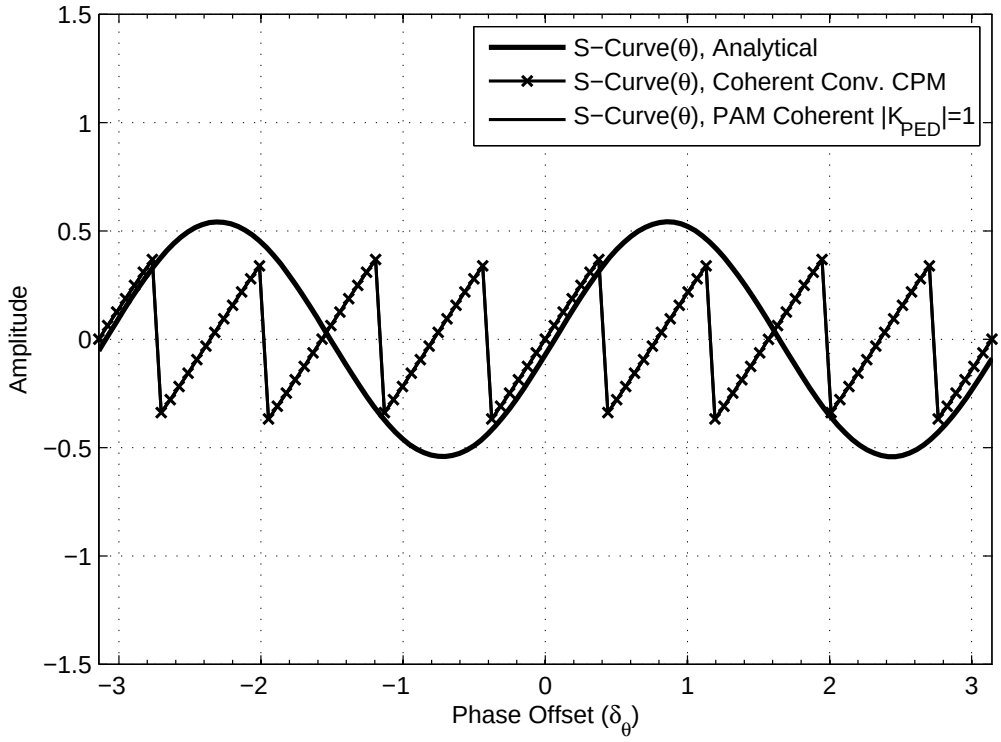

Figure 6.7. S-Curves for the PED. The modulation scheme is Quaternary CPM ($M = 4$, $L = 2$, $h = 1/4$).

1 pulse in the PAM based TED for coherent and noncoherent detections are considered for comparison. The coherent TEDs show better tracking accuracy compared to the noncoherent TEDs by operating very close to the practical lower limits of the MCRB(τ). We also observe that the tracking accuracy of the reduced-complexity TEDs are very much comparable to the original implementation of the conventional CPM TED. Also, the tracking performance of all the reduced-complexity configurations are quite good for small values of E_s/N_0, but, at higher values of E_s/N_0, they deviate from the MCRB(τ) due to the internal noise in the DD algorithm. In this example, for the coherent case, the relative ranking between the reduced-complexity TED configurations often fluctuates depending on the operating range of E_s/N_0 but in general a TED with 2 pulses offers similar or better tracking performance when compared to a TED with 1

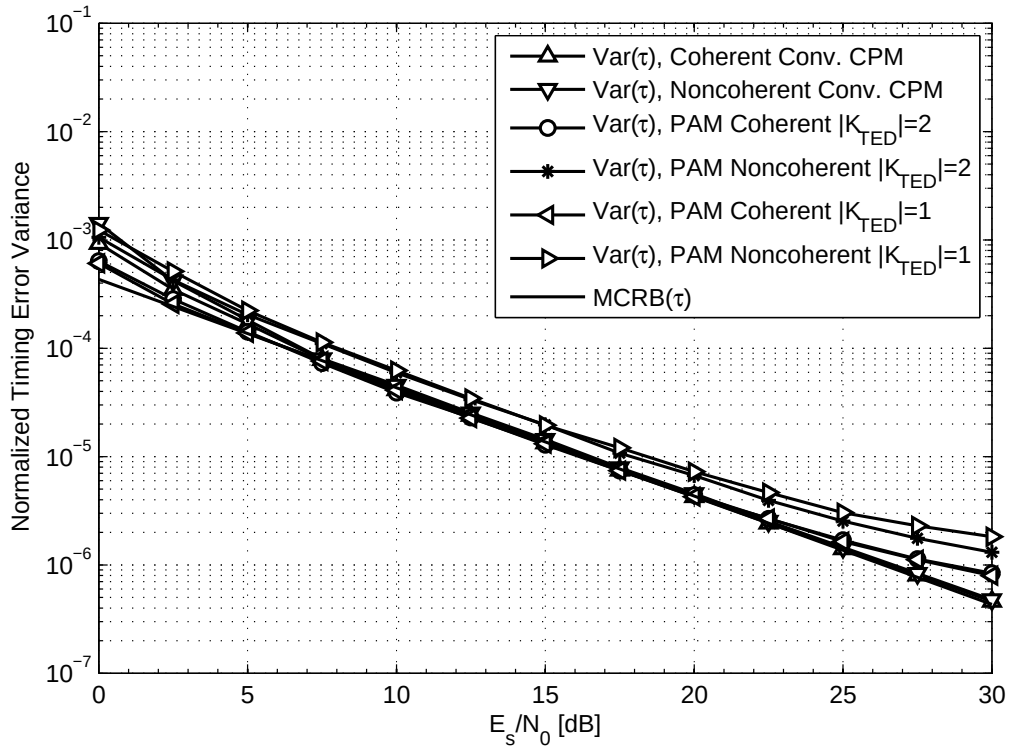

Figure 6.8. MCRB vs. normalized timing error variances for the TED. The modulation scheme is CPM ($M = 4$, 2RC, $h = 1/4$) with $B_\tau T_s = 1 \times 10^{-3}$.

pulse. This is readily visible for the noncoherent case, where the 2 pulse TED offers a slightly better tracking performance than the 1 pulse TED, especially for higher E_s/N_0. Both noncoherent PAM based TEDs operate about 1 to 2 dB away from the MCRB(τ).

Next, in Figure 6.9, we compare the phase error variance of the PED for the conventional CPM and the PAM based implementations. We also compare cases with 2 pulses and 1 pulse in the PAM based PEDs for coherent detections. We observe that the tracking accuracy of the reduced complexity PEDs are very much comparable to the original implementation of the conventional CPM PED, especially for lower values of E_s/N_0. At large values of E_s/N_0 it deviates further away from the MCRB(θ) which is due to the internal noise generated by the DD algorithm. We employ only a first-order PLL for phase acquisition and tracking in this case also. In this example, the relative

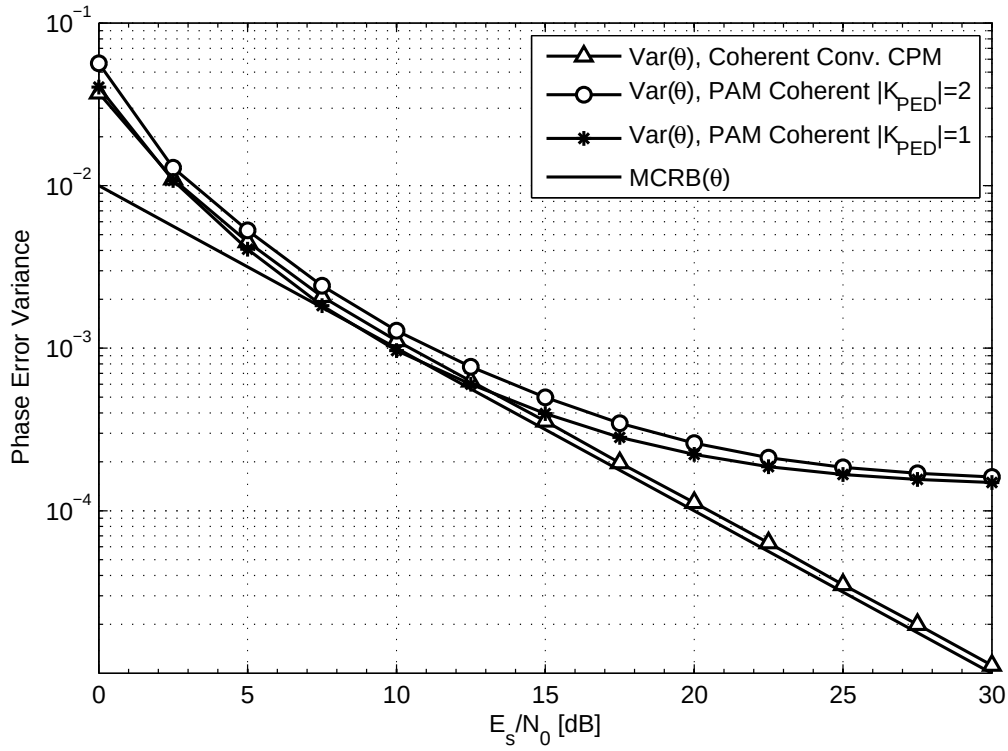

Figure 6.9. MCRB vs. phase error variances for the PED. The modulation scheme is CPM ($M = 4$, 2RC, $h = 1/4$) with $B_\theta T_s = 1 \times 10^{-2}$.

ranking between the reduced-complexity PED configurations often fluctuate depending on the operating range of E_s/N_0. The PED with 1 pulse offer slightly better tracking performance than the PED with 2 pulses which is in contrast with the corresponding TED cases.

Finally, we compare the bit error rates shown in Figure 6.10 for the conventional CPM and the PAM based configurations. The coherent conventional CPM receiver has the lowest BER and is similar or slightly worse in most part as the theoretical BER for this scheme for AWGN channel. The conventional noncoherent CPM receiver comes next; operating only within about 0.5 dB off the coherent receiver at a probability of error of 10^{-4}. The reduced-complexity PAM based receivers all show good BER and vary within 1 dB of the theoretical value at a given probability of error. We notice

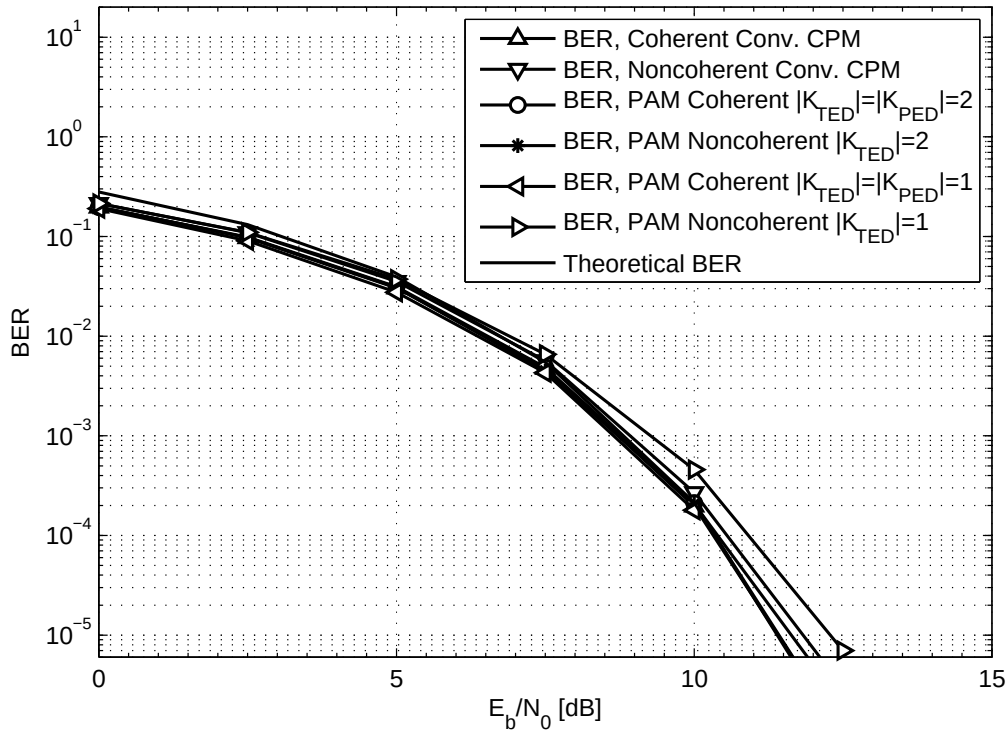

Figure 6.10. Theoretical BER vs. BER obtained for various conventional and PAM based implementations of the CPM scheme ($M = 4$, 2RC, $h = 1/4$) with $B_\tau T_s = 1 \times 10^{-3}$ and $B_\theta T_s = 1 \times 10^{-2}$.

a performance improvement here for the detector with 1 pulse TED compared to the GMSK modulation observed previously.

6.1.3 Observation Summary

A comparative study of the results we found in this chapter are now summerized in Table 6.1 and Table 6.2.

They show that, for a given E_s/N_0, the PAM based receiver performance is comparable to that of the conventional CPM receiver for different MF pulse and trellis configurations. We also observe that though the tracking variance for timing operates very close to the MCRB for most of the input E_s/N_0 range, such is not the case with phase

Table 6.1. BER and Tracking Error Variance performance comparison For GMSK with an input E_s/N_0 of 10 dB in AWGN channel.

Modulation	Error Variance(τ)	Error Variance(θ)	BER
Coherent (C) CPM	8.21×10^{-5}	0.25×10^{-2}	2.55×10^{-4}
CPAM $\lvert\mathcal{K}_{\text{TED}}\rvert = \lvert\mathcal{K}_{\text{PED}}\rvert = 2$	8.25×10^{-5}	0.85×10^{-3}	2.54×10^{-4}
CPAM $\lvert\mathcal{K}_{\text{TED}}\rvert = \lvert\mathcal{K}_{\text{PED}}\rvert = 1$	8.39×10^{-5}	0.85×10^{-3}	40.25×10^{-4}
Noncoherent (NC) CPM	8.41×10^{-5}	N/A	3.05×10^{-4}
NCPAM $\lvert\mathcal{K}_{\text{TED}}\rvert = 2$	9.57×10^{-5}	N/A	3.25×10^{-4}
NCPAM $\lvert\mathcal{K}_{\text{TED}}\rvert = 1$	1×10^{-4}	N/A	40.25×10^{-4}

Table 6.2. BER and Error Tracking Variance performance comparison for a 4-ary CPM with an input E_s/N_0 of 10 dB in AWGN channel.

Modulation	Error Variance(τ)	Error Variance(θ)	BER
Coherent (C) CPM	2.84×10^{-4}	1.01×10^{-3}	0.95×10^{-4}
CPAM $\lvert\mathcal{K}_{\text{TED}}\rvert = \lvert\mathcal{K}_{\text{PED}}\rvert = 2$	2.88×10^{-4}	1.23×10^{-3}	0.94×10^{-4}
CPAM $\lvert\mathcal{K}_{\text{TED}}\rvert = \lvert\mathcal{K}_{\text{PED}}\rvert = 1$	3.48×10^{-4}	9.86×10^{-4}	0.97×10^{-4}
Noncoherent (NC) CPM	3.57×10^{-4}	N/A	1.15×10^{-4}
NCPAM $\lvert\mathcal{K}_{\text{TED}}\rvert = 2$	5.57×10^{-4}	N/A	1.25×10^{-4}
NCPAM $\lvert\mathcal{K}_{\text{TED}}\rvert = 1$	5.61×10^{-4}	N/A	3.85×10^{-4}

as it starts to deviate about halfway through the input E_s/N_0 range. Also, interestingly, the $|\mathcal{K}_{\text{PED}}| = 2$ PAM based system seem to have worse phase tracking efficiency than the $|\mathcal{K}_{\text{PED}}| = 1$ pulse PAM receiver. However, the BER is not affected by a large amount by this relative lack of efficiency in phase tracking. Both coherent PAM receivers provide BERs close to the theoretical value of 10^{-4} for the input $E_s/N_0 = 10$ dB as seen from the table.

6.2 Perfomance of PAM Based Receivers Under Large Frequency Offsets

We again present a comprehensive comparative study of the existing conventional CPM and PAM based receivers of binary and M-ary CPM systems under the assumption that there is a large frequency offset on the order of the symbol rate present due to

the Doppler shift in the channel or the oscillator instabilities between transmitter and receiver.

In Section 5.2, we explained why coherent detection in the presence of a large frequency offset can be quite difficult. In this section, we actually show the results of the PAM based coherent and noncoherent detection under a large carrier frequency offset. For coherent detection, we keep the phase PLL second-order as the second-order PLL is suitable in situations where there is a small carrier frequency offset. However, after the frequency recovery, the residual frequency offset in the carrier is still around 2% to 3% of the symbol rate. The results obtained through simulations confirm that coherent detection is not suitable for symbol recovery under large frequency offsets, even with the initial frequency recovery. This is due to large error in phase acquisition under the presence of frequency offsets. Simulations show that, any frequency offset of more than $10^{-4}T_s$ causes phase PLL to loose the lock. The timing lock, however still remains attainable. Therefore, it is more feasable to use noncoherent detection. Another reason behind opting for the noncoherent detection is that, it is usually inferior to its coherent counterpart (under no frequency offset condition) by only about 1 dB to 2 dB in terms of error tracking and BER performances as we have shown in Section 6.1.

6.2.1 Binary GMSK Under a Large Frequency Offset: $M = 2$, $L = 4$, $h = 1/2$

We first apply the NDA PAM based frequency recovery algorithm for the binary GMSK scheme with $M = 2$, L=4, and $h = 1/2$ and $B = 1/4$. By simulation we found that, only keeping a single MF pulse is sufficient for the FDD described in Section 3.3. We also use a delay and multiply based FDD scheme for CPM described in [20] and use it in the conventional CPM receiver for comparing the performance against the PAM based CPM receivers.

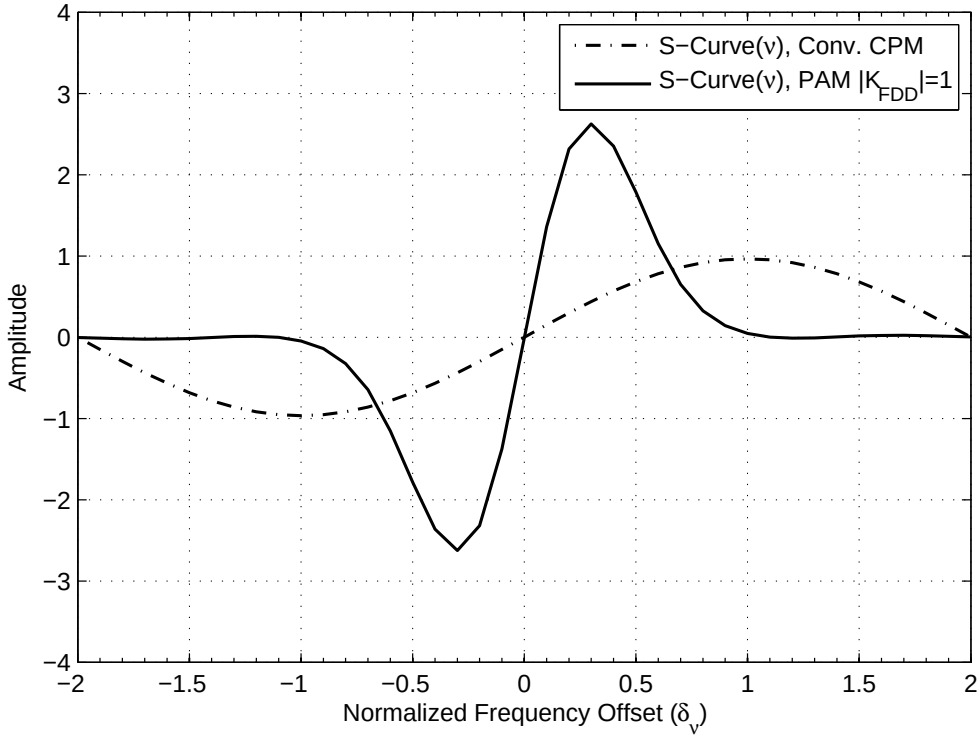

Figure 6.11. S-Curves for the FDD. The modulation scheme is GMSK ($M = 2$, $L = 4$, $h = 1/2$, $B = 1/4$).

Figure 6.11 shows that the S-curve of the PAM based FDD has a lock point at zero and no false lock points which is true for any NDA scheme. We also observe that the S-curve is linear within about ± 0.35 of the symbol rate which is quite a large lock range. Out of a number of reduced-complexity PAM based detector configurations, we select a 4-state detector with $L' = 2$ that uses a bank of $|\mathcal{K}| = |\mathcal{K}_{\text{TED}}| = 2$ MFs/pulses and $|\mathcal{K}_{\text{TED}}| = 1$ pulse respectively and then compare their detection and tracking efficiencies with that of the conventional noncoherent CPM scheme.

Figure 6.12 shows the normalized timing error variances of the noncoherent PAM based and conventional CPM detectors. We select a 4-state PAM based detector with $L' = 2$ that uses a bank of $|\mathcal{K}| = |\mathcal{K}_{\text{TED}}| = 2$ MFs/pulses and $|\mathcal{K}_{\text{TED}}| = 1$ pulse respectively and then compare their detection and tracking efficiencies with that of the

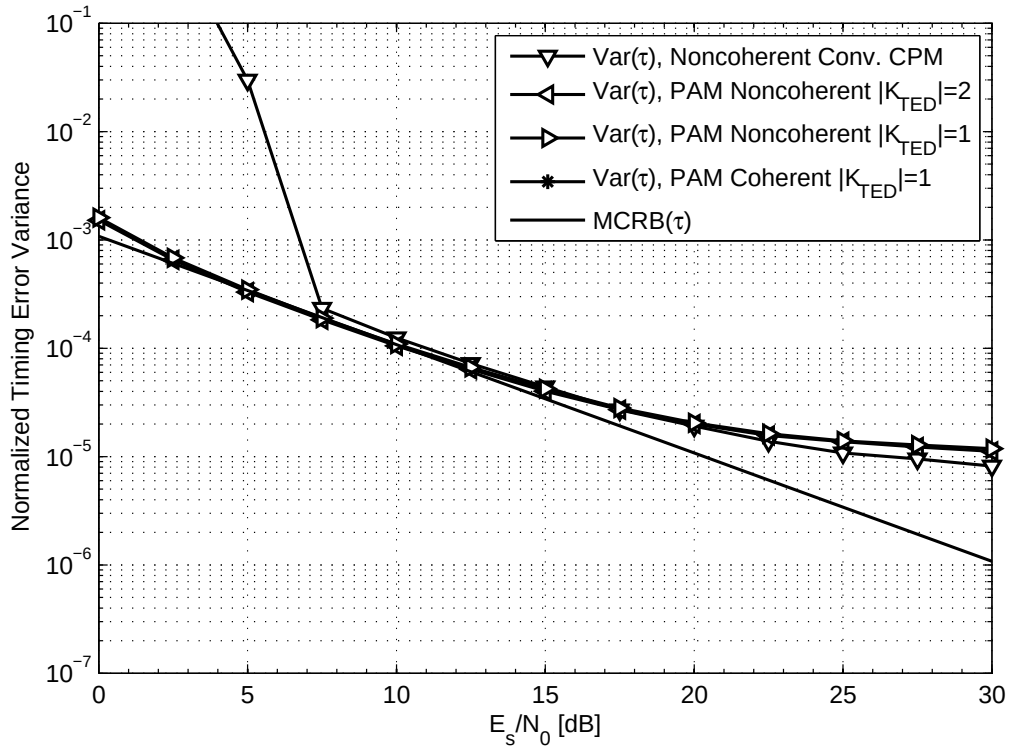

Figure 6.12. MCRB vs. normalized timing error variances for the TED. The modulation scheme is GMSK ($M = 2$, $L = 4$, $h = 1/2$, $B = 1/4$) with $B_\tau T_s = 1 \times 10^{-3}$.

conventional noncoherent CPM scheme.

Figure 6.13 shows the frequency error variances of the NDA PAM based and conventional CPM detectors. The conventional CPM-FED performs marginally better than the PAM-FED.

Figure 6.14 shows the BERs of the PAM based and conventional CPM detectors under a large frequency offset. The noncoherent conventional CPM performs better than noncoherent PAM with $|\mathcal{K}| = |\mathcal{K}_{\text{TED}}| = 2$ MFs/pulses and $|\mathcal{K}_{\text{TED}}| = 1$ pulse by about 1.7 dB at a BER of 10^{-5}. The coherent PAM with $|\mathcal{K}_{\text{TED}}| = |\mathcal{K}_{\text{PED}}| = 1$ pulse, however, performs the worst.

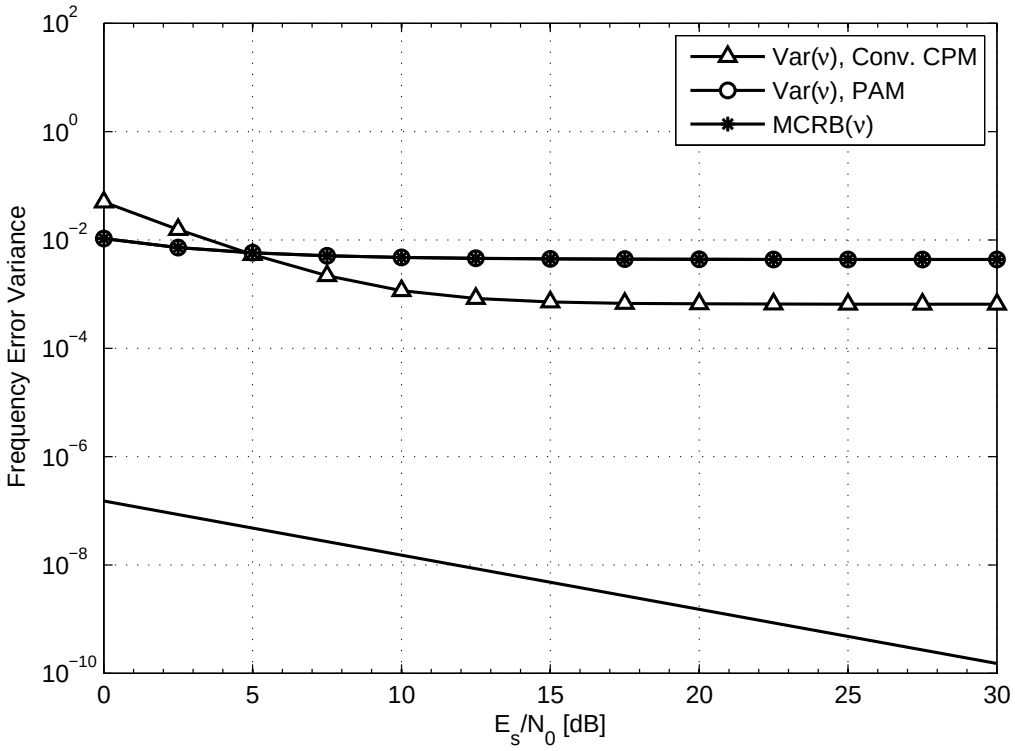

Figure 6.13. MCRB vs. normalized frequency error variances for FDD. The modulation scheme is GMSK ($M = 2$, $L = 4$, $h = 1/2$, $B = 1/4$) with $B_\nu T_s = 5 \times 10^{-3}$.

6.2.2 Quaternary CPM Under a Large Frequency Offset: $M = 4$, 2RC, $h = 1/4$

We first describe the NDA conventional and PAM based frequency recovery schemes for the quaternary CPM scheme with $M = 4$, $L = 2$, and $h = 1/2$. By simulation we found that, only keeping a single pulse is sufficient for the FDD described in Section 3.3. We also apply one conventional CPM based FDD scheme cited in [20] and use it as a reference to compare the performance against PAM based noncoherent receiver under a large frequency offset.

The S-curves in Figure 6.15 show that the PAM S-curve has only one lock point at zero and no false lock points which is true for any NDA scheme. It is also observed that the S-curve is linear within about 0.7 of the symbol time with is quite a large lock

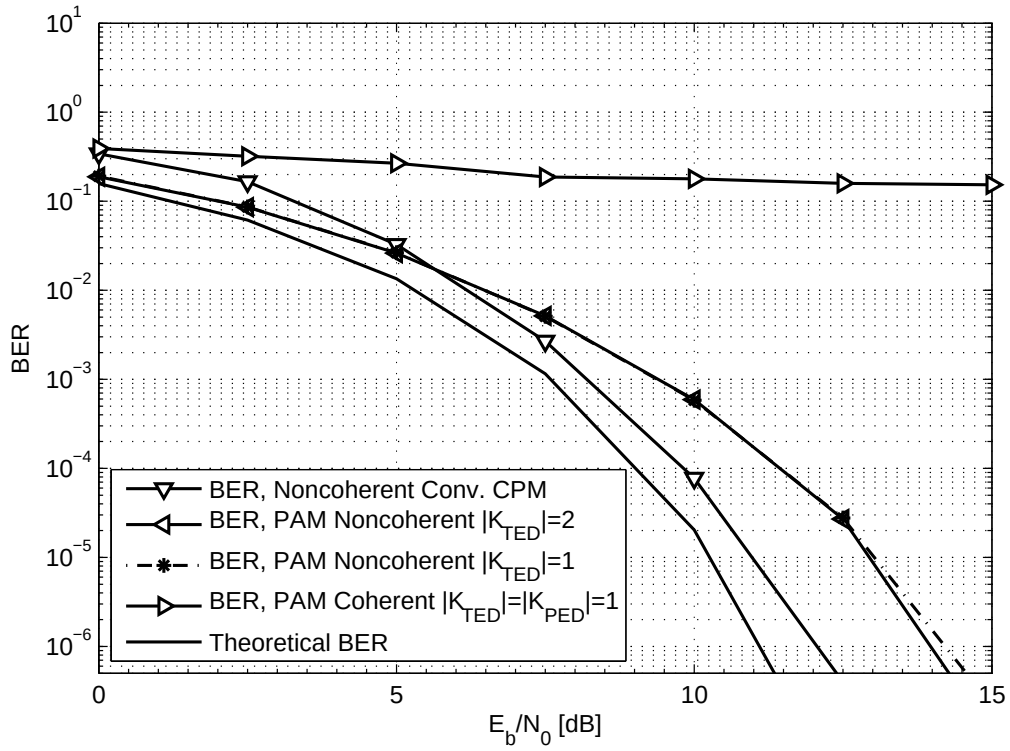

Figure 6.14. Theoretical BER vs. BER obtained for various conventional and PAM based implementaions with the initial carrier frequency recovery.The modulation scheme is GMSK ($M = 2$, $L = 4$, $B = 1/4$ $h = 1/2$) with $B_\tau T_s = 1 \times 10^{-3}$ and $B_\nu T_s = 5 \times 10^{-3}$.

range. Out of a number of reduced-complexity PAM based detector configurations, we select a 4-state detector with $L' = 1$ that uses a bank of $|\mathcal{K}| = |\mathcal{K}_{\text{TED}}| = 2$ MF/pulses and $|\mathcal{K}_{\text{TED}}| = 1$ pulse respectively. We then compare their detection and tracking efficiencies to that of the conventional noncoherent CPM scheme.

Figure 6.16 shows that the noncoherent CPM-TED and PAM-TED offer much lower tracking variances than their corresponding coherent counterparts. Figure 6.17 shows that the conventional CPM-FED performs better than the PAM-TED but both perform far away from the MCRB(ν).

We simulate the coherent conventional CPM and PAM based systems under a large

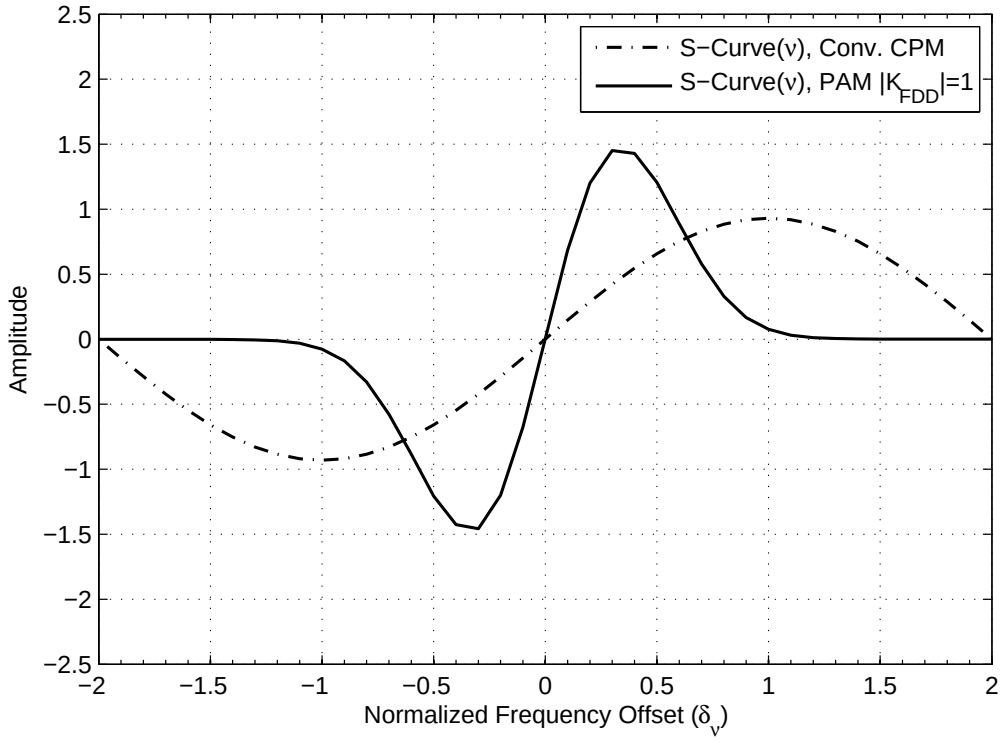

Figure 6.15. S-Curves for the FDD. The modulation scheme is M-ary CPM ($M = 4$, 2RC, $h = 1/4$).

frequency offset condition and they provide much worse BER than the noncoherent schemes as seen from Figure 6.18. This is due to inadequate phase tracking under even a small amount of frequency offset. The carrier phase is affected a lot more by the introduction of the frequency offset as compared to the symbol timing.

6.2.3 Observation Summary

We summarize a comparative study of the results we found in this section in the following tables.

Table 6.3 and 6.4 show that for a given input E_s/N_0, the PAM based receivers with various MF/TED pulse and trellis configurations are comparable in performance to the conventional CPM receivers for noncoherent detection. The results also indicate

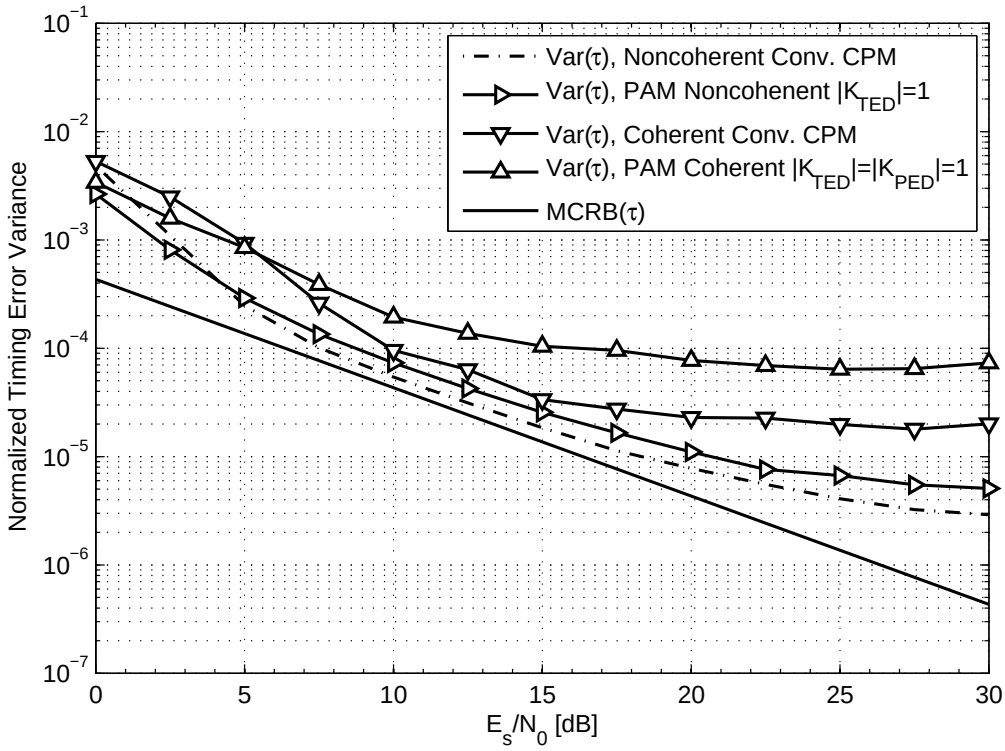

Figure 6.16. MCRB vs. normalized timing error variances for the TED. The modulation scheme is M-ary CPM ($M = 4$, 2RC, $h = 1/4$) with $B_\tau T_s = 1 \times 10^{-3}$.

Table 6.3. BER and Variance performance comparison for GMSK with an input E_s/N_0 of 10 dB in AWGN channel.

Modulation	Error Variance(τ)	Error Variance(ν)	BER
Noncoherent (NC) CPM	1.21×10^{-4}	2.5×10^{-4}	8.15×10^{-4}
NCPAM $\lvert\mathcal{K}_{\text{TED}}\rvert = 1$	1×10^{-4}	1.5×10^{-3}	43.5×10^{-4}

a marked degradation in the system performance in the presence of large frequency offsets. The FDD algorithm, although has a relatively higher lock range and does not require being driven by decisions or actual data, it introduces enough jitter due to its noisy tracking process that, it affects the noncoherent system performance by as much as 3 dB.

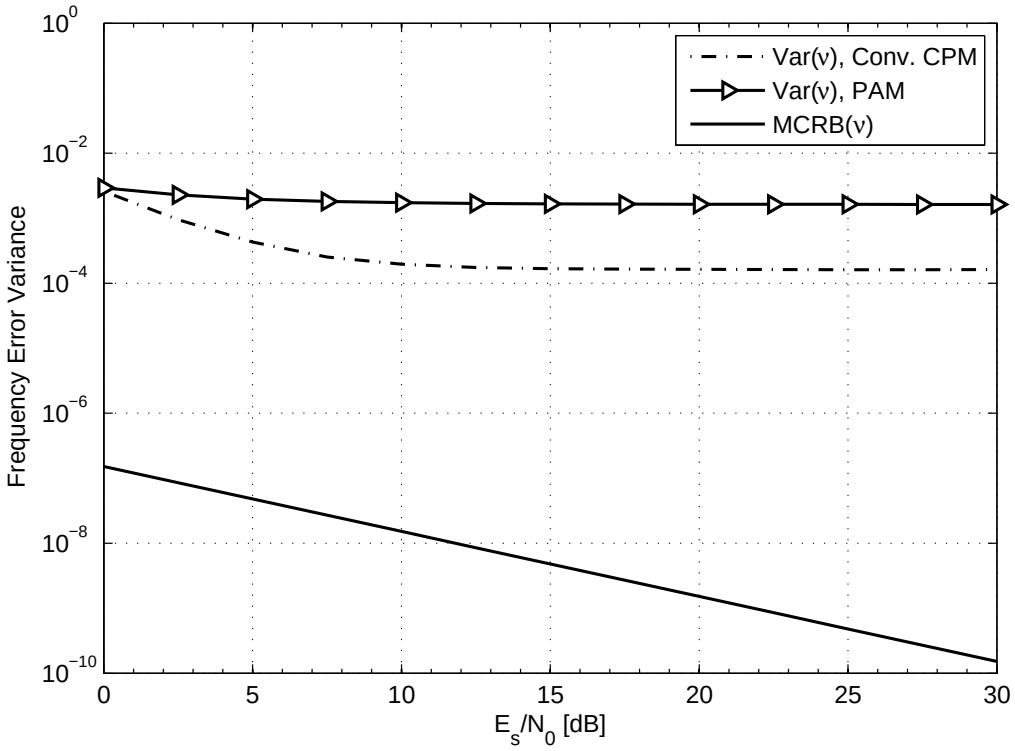

Figure 6.17. MCRB vs. normalized frequency error variances for the FDD. The modulation scheme is M-ary CPM ($M = 4$, 2RC, $h = 1/4$) with $B_\nu T_s = 1 \times 10^{-3}$.

Table 6.4. BER and Variance performance comparison for a 4-ary CPM for an input E_s/N_0 of 10 dB in AWGN channel.

Modulation	Error Variance(τ)	Error Variance(ν)	BER
Noncoherent (NC) CPM	5.41×10^{-5}	1.96×10^{-4}	4.57×10^{-4}
NCPAM $\lvert\mathcal{K}_{\text{TED}}\rvert = 1$	7.31×10^{-5}	1.73×10^{-3}	6.75×10^{-4}
Coherent (C) CPM	9.56×10^{-5}	1.96×10^{-4}	5.07×10^{-3}
CPAM $\lvert\mathcal{K}_{\text{TED}}\rvert = 1$	1.93×10^{-4}	1.73×10^{-3}	2.13×10^{-2}

6.3 Key Points and Recommendations

Based upon the simulation results presented in this chapter, we can infer that

• PAM based reduced-complexity CPM detectors provide very good tracking characteristics under no carrier frequency offset.

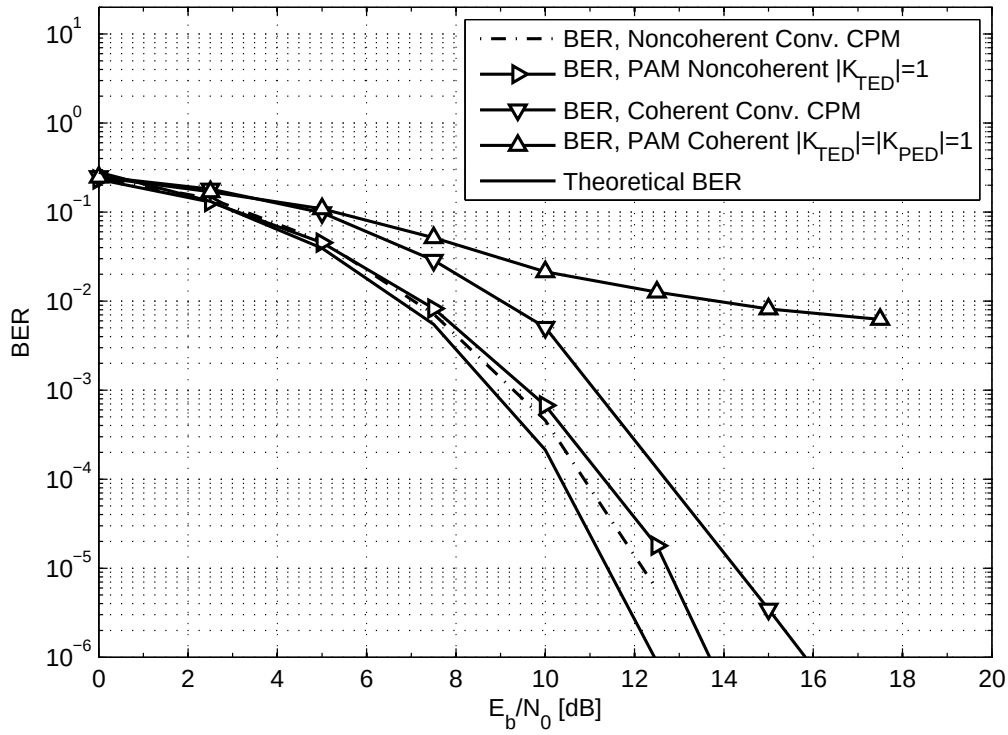

Figure 6.18. Theoretical BER vs. BER obtained for various conventional and PAM based implementaions with the initial carrier frequency recovery. The modulation scheme is M-ary CPM ($M = 4$, 2RC, $h = 1/4$) with $B_\tau T_s = 1 \times 10^{-3}$ and $B_\nu T_s = 5 \times 10^{-3}$.

• Coherent and noncoherent detection can be done based on PAM based detectors. The noncoherent detectors are worse by about 2 dB in BER under all practical requirements and under no frequency offset condition.

• With a frequency offsets on the order of 10^{-4} of the symbol rate, the performance of PAM based detectors does not suffer deterioration in terms of tracking accuracy and BER.

• With the carrier frequency offset on the order of the symbol rate, noncoherent detection outperforms coherent detection in terms of tracking accuracy and BER.

• Frequency detectors are non-data-aided, thereby causing a relatively large residual

frequency jitter which can be further removed by methods discussed in [14], if coherent detection is used. However, noncoherent detection allows further simplification of the receiver structure by alleviating the need for a second stage of frequency recovery, although more investigation on this is required.

- Algorithms discussed in this thesis are simple to implement and comparable in performance to conventional CPMs. They reduce the complexity of the CPM receivers and have good timing, phase and frequency synchronization components making them an alternative option for commercial cost-effective receivers.

Chapter 7

Timing False Lock Recovery with M-ary CPM

So far, we have discussed and compared simulation results for both conventional and PAM based receivers under the steady-state condition. In this chapter, we concentrate on the acquisition characteristic of the synchronizers. We propose a suitable solution to a common problem during acquisition, i.e., the false lock problem. This is another important contribution of this thesis.

7.1 False Lock with No Frequency Offset

Under no carrier frequency offset, the steady-state results indicated very good tracking performance for both conventional and PAM based synchronizers. However, the acquisition behavior may be different for them. In fact, it can be found by simulation that, depending on the modulation format, the timing and/or phase synchronizers get into false locks which was earlier described in [12]. This happens only with M-ary partial response formats. A simple explanation for the false lock is that the decision-

Table 7.1. BER and Variance performance comparison of M-ary CPM under spurious lock with input $E_s/N_0 = 12$ dB.

Metric	Value by Simulation	Theoretical
BER	0.2808	0
Timing Variance	0.5007×10^{-3}	0.0511×10^{-3}
Phase Variance	0.0397	0.0006

directed timing and phase recovery use ML method to find the location of the maximum of (5.2) and (5.3) in the $(\tilde{\tau}, \tilde{\theta},)$ plane with the assumption that a reliable estimate of the data sequence $\tilde{\boldsymbol{\alpha}}$ is available from the VA. It appears that the functions which they try to maximize are not monotonic (increasing or decreasing) and consequently have several local peaks along with one global maximum. Spurious or false locks occur when the algorithm tends to settle on one of the local peaks from the initial conditions. This can be analogically related to a marble on top of a convex side of a curved floor that has several concave structures. When the marble is moved a little from its unstable position, it tries to go to the closest minimum point on the surface, regardless of whether it is a local minimum or the global minimum. A case of this false lock problem was shown in [12] for a quaternary 3RC CPM scheme with a modulation index of $1/2$ and is reproduced here for illustration purpose.

Figure 7.1 shows a situation of occurrence of a spurious lock. The timing estimate gets locked onto a value of -0.35 and phase wanders around a value of -1.6 radians. Typical values of the BER, timing and phase variances under the false lock situation are shown in Table 7.1.

Table 7.1 shows that under a spurious lock the system has fairly high timing and phase tracking variances and its BER is about $1/3$, which shows poor system performance. In [12], a non data aided "auxiliary" lock detector is employed. While it does detect a false lock and removes it, it has some distinct disadvantages: it is slow, noisier due to its NDA nature and has a longer acquisition time.

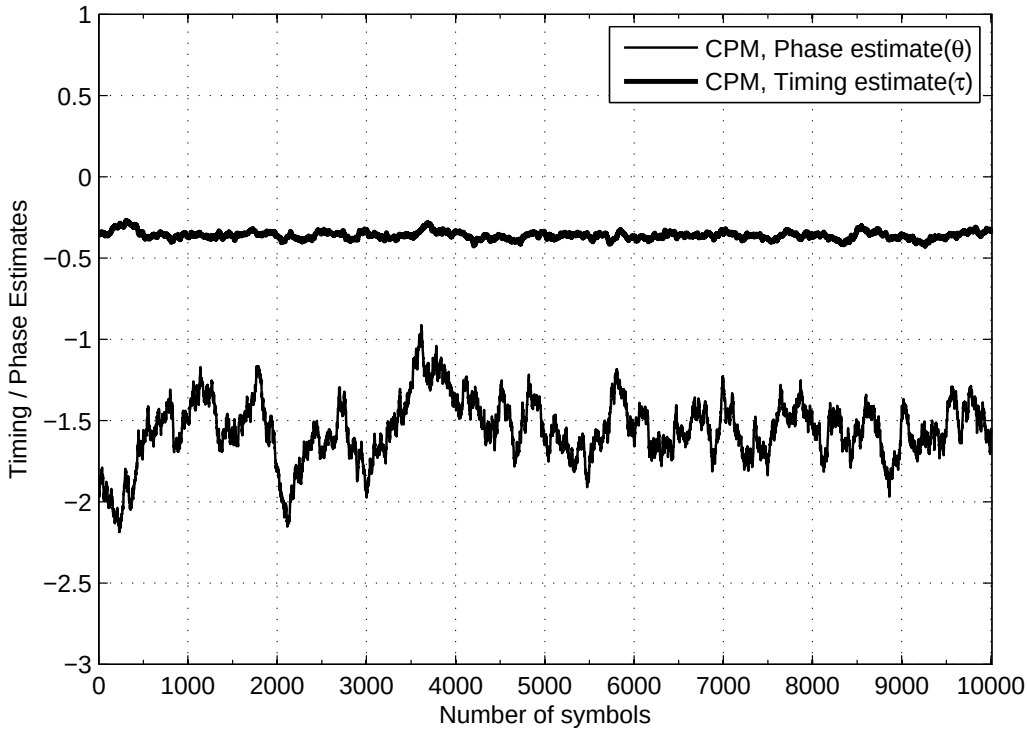

Figure 7.1. Timing and Phase estimates for $M = 4$, $3RC$, $h = 1/2$ with $B_\tau T_s = 5 \times 10^{-3}$ and $B_\theta T_s = 5 \times 10^{-2}$.

In this thesis, we observe a simple solution to the false lock problem. The variable lengths of the PAM based matched filters impart extra "variation" to the system whereby any false lock, if occurs, can be eventually removed. This is promising because the proposed receiver does not use any additional lock recovery circuitry and is suitable for use with faster decision-directed algorithms. During several simulations runs it is observed that, a noncoherent synchronizer with only 1 TED pulse does very well to keep the system from falling into a false lock. Also, 2 pulse coherent and noncoherent synchronizers do reasonably well. This can be attributed to lower peaks at the false lock points for the PAM based TED system as compared to the conventional CPM based system as shown in Figure 7.2. These lower peaks and lesser slopes, combined with the internal noise in the algorithm due to varied MF lengths, help drive the system

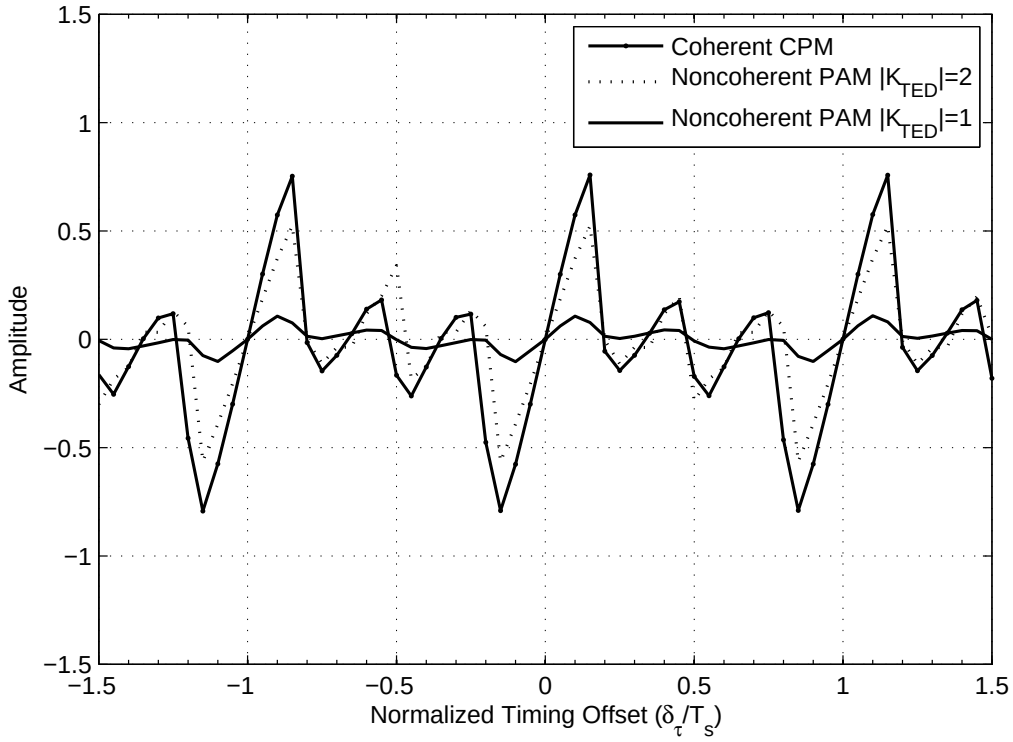

Figure 7.2. S-curves of the noncoherent CPM and the PAM based TEDs.

out of the false lock. In our simulations, we focus mainly on the noncoherent PAM based TED with 1 pulse as this provides the best result.

From Figure 7.2 it is observed that the noncoherent PAM based system with 1 TED pulse has the lowest slope around the false lock points and consequently, the largest step size. Therefore, its probability of getting out of a spurious lock is more than the other TEDs shown in the figure. With the conventional CPM-TED, we run a simulation of 100000 times and plot the lock acquisition time distribution. Figure 7.3 shows that there is a large number of cases, represented by the solid virtical section at the end of the figure, where the conventional CPM system is unable to recover from false locks and therefore, is unsuitable for use.

In the PAM based system shown in Figure 7.4, the simulation is run independently

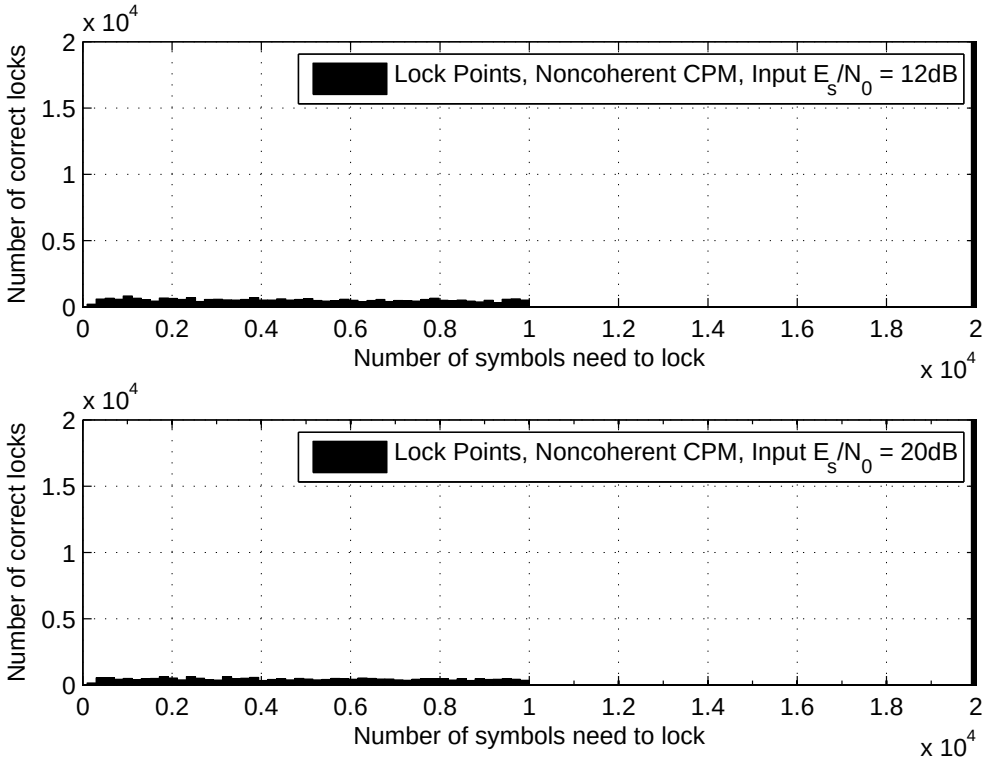

Figure 7.3. False lock trials (noncoherent 1 pulse TED) for $M = 4$, 3RC, $h = 1/2$ and $BT_s = 5 \times 10^{-3}$.

100000 times and the lock acquisition time distribution is plotted. It appears similar to an exponential distribution with mean lock acquisition point is within about 700 symbol periods. In comparison to the conventional CPM scheme, there are very few cases where the PAM based system is unable to avoid the false lock. In particular, only 30 cases out of the 100000 independent trials, the system was unable to recover from the false lock; thus providing a very low false lock probability of 0.03%. The situation gets worse a little as we increase the input E_s/N_0. The PAM based system shows 0.089% false lock at an input E_s/N_0 of 20 dB, still, much better than the conventional CPM system under similar condition. The result varies minutely across different modulations schemes. We found, by simulation that, for all realizable CPM schemes, the PAM based noncoherent single pulse TED guarantees that any spurious lock will

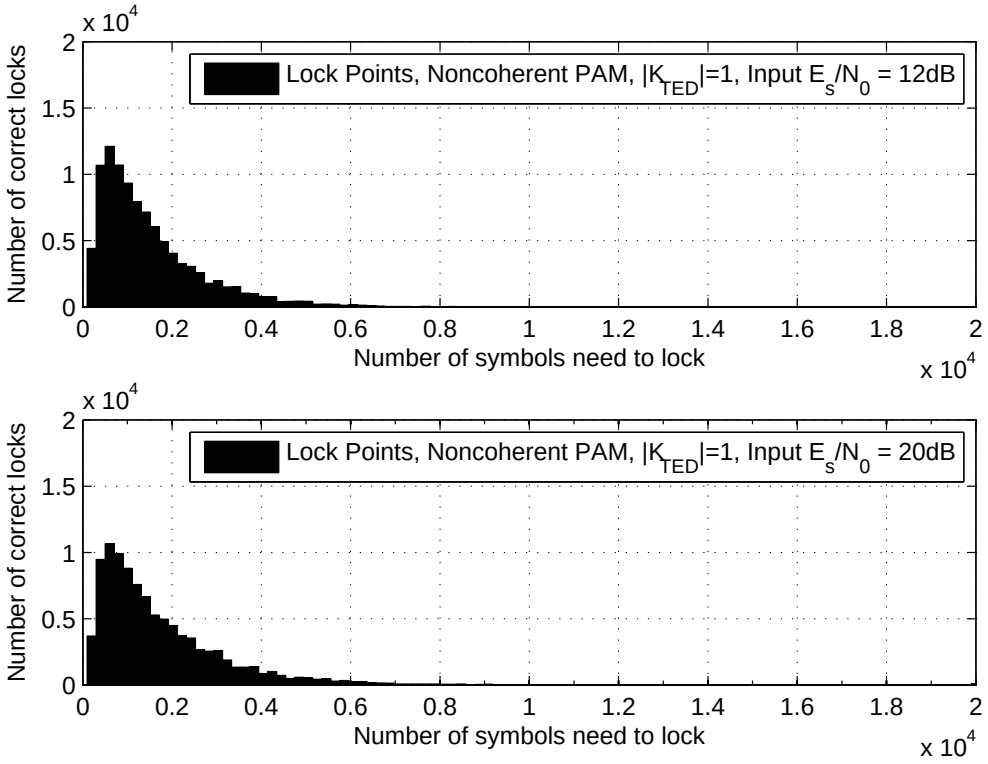

Figure 7.4. False lock trials (noncoherent 1 pulse TED) for $M = 4$, 3RC, $h = 1/2$ and $BT_s = 5 \times 10^{-3}$.

be removed, or, at least the probability of false lock will be confined to a negligible amount. Compared to a similar conventional CPM scheme, this is a huge improvement in the acquisition performance. Therefore, our approach shows that, a simple reduced-complexity PAM based noncoherent single pulse TED system can be employed without any extra circuitry for guaranteed performance improvement in terms of the spurious lock removal, when compared to a similar conventional CPM scheme.

7.2 False Lock Under a Large Carrier Frequency Offset

While discussing joint frequency, timing and phase recovery in Chapter 5, we mentioned that after the frequency lock is achieved, the internal noise of the NDA frequency

acquisition algorithm introduces a residual frequency offset that can not be completely removed from the signal before it is fed to the timing and phase DD synchronizers. The small frequency offset introduces extra noise in the system which helps reduce further the false lock probability. Returning to the marble analogy, the additional noise prevents the marble from settling easily in local minima and ultimately helps it find the global minimum. Simulation results with various CPM schemes confirm our prediction. Interestingly, in the presence of a small (2% to 3% of the symbol rate) frequency offset, conventional CPM receivers in noncoherent mode perform equally well to their PAM based single TED counterparts when it comes to avoiding the false lock. But, overall, in a complete tracking environment where the incoming frequency, phase and timing information are unknown to the receiver, our PAM based model ensures a very low probability of false locks, as shown in Table 7.2.

Figure 7.5 presents a comparison of timing lock acquisitions in the presence of a frequency offset for conventional CPM and PAM based noncoherent receivers with single TED pulse. Compared to Figure 7.4 discussed in the previous section, the conventional CPM system does provide a comparable performance against our PAM based system. We did 100000 independent trial runs with a frequency offset of about 3×10^{-3} of the symbol rate and found no false lock occurrences for both conventional and PAM based systems. Therefore, a small frequency offset appears to add enough extra noise to both the systems so that, it helps them avoid false locks.

We summarize the results discussed in Section 7.1 and in Section 7.2 in the following Table 7.2.

Table 7.2 shows that, the solution to the false lock problem lies in the internal noise in the system itself! we observe that there are little or no false locks if we use a noncoherent single pulse PAM-TED receiver. Introduction of a small frequency offset ben-

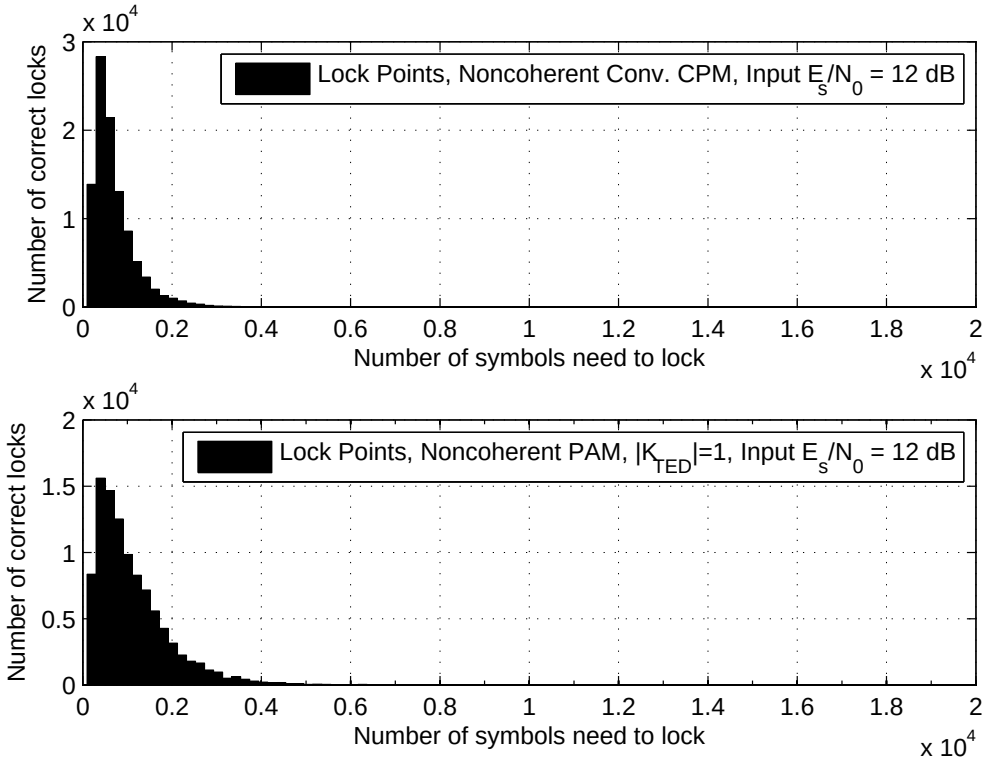

Figure 7.5. False lock trials (noncoherent 1 pulse TED) for $M = 4$, 3RC, $h = 1/2$ and $B_\tau T_s = 5 \times 10^{-3}$.

efits both CPM and PAM based system in the fact that, both systems are now able to act without getting into spurious locks. So, in general, reduced-complexity PAM based receivers produce consistent performance under false lock conditions with or without carrier frequency offsets. We conclude this chapter by pointing out the fact that a trade-off exists between the choice of the PAM pulses in the TED and its ability to recover from false lock during acquisition. A single pulse TED is best when avoiding a false lock is of prime importance, whereas, a 2 pulse TED provides slightly better tracking accuracy and BER.

Table 7.2. Performance comparison - timing lock recovery $M = 4$, 3RC, $h = 1/2$ and $B_\tau T_s = 5 \times 10^{-3}$ under false lock.

No Frequency Offset	NC conventional	NC PAM $\lvert\mathcal{K}_{\text{TED}}\rvert = 1$
No. of Simulations	10^5	10^5
No. of False locks	10^5	30
False lock probability	1	0.0003
Lock state	No lock	Consistent over no. of symbols
Small Frequency Offset	NC conventional	NC PAM $\lvert\mathcal{K}_{\text{TED}}\rvert = 1$
No. of Simulations	10^5	10^5
No. of False locks	0.0	0.0
False lock probability	0.0	0.0
Lock state	Consistent	1 or 2 momentary loss

Chapter 8

Conclusions and Future Work

We have shown how the PAM representations of binary as well as M-ary CPMs can be applied to the problem of *joint* carrier frequency, carrier phase and symbol timing recovery for reduced-complexity CPMs in general. We have developed formulations for joint operation of PAM based TEDs and PEDs, and also incorporated FDDs to analyze and compare their performances under various offset conditions in timing, phase and frequency. From the simulation results it is confirmed that the PAM based CPM receivers provided a comparable performance against conventional CPM receivers and proved to be a better choice where there is a possibility of spurious locks. We also have analyzed the possibility of noncohrerent detection for the PAM based receivers have shown superiority over their coherent counterpart when there is a large carrier frequency offset present. Therefore, this thesis considers all possible signal recovery scenarios for CPM transmission over AWGN channel and provides important *joint* synchrozation components for recovering carrier frequency, symbol timing and carrier phase of the signal that have been missing up to this point.

The future work will include looking into the possibility of noncoherent detection and eliminate the need for a second frequency offset synchronizer which is used to

further improve the frquency recovery of the signal. A comparative study of system performance with out the second synchronizer is essential to determining the effectiveness of the solution.

There is also a possibiity of looking further into the false lock recovery solution we proposed and try out various combinations of PAM pulses to see if the system recovers from it completly without the need of any extra lock detector. For example, having a single pulse noncoherent TED during initial acquisition of the symbol timing and reverting to a two-pulse noncoherent TED when the timing lock is acquired, could improve the acquisition and tracking performance of the error detectors greatly.

Finally, the performance of the proposed algorithms have only been described in AWGN channel where the channel frequency response remains constant over the entire transmission length. The behavior of the *joint* synchronizers under steady-state as well as acquisition stages can be further explored for fading channels and provide a detailed understanding of the algorithms under the most practical considerations.

8.1 Sponsor Acknowledgement

We would like to thank Nokia-Siemens Networks and the University of Kansas General Research Funds for their partial support throughout this research.

Appendix A

Calculation of S-Curves

In this appendix, we present some useful derivations and implementation methodologies for the S-curves we discussed previously in Section 4.3.

A.1 Timing S-Curve

We now give a derivation in fair detail of the S-curve for the timing TED assuming that, we know the transmitted symbol sequence $\boldsymbol{\alpha}$ (i.e. the *data-aided* case).

To proceed, we make use of the fact that, the S-curve deals only with the difference between original and estimates and use the substitution $\delta_\tau = \tau - \hat{\tau}$ to replace τ, with $\hat{\tau} = 0$ to further simplify the analysis. Inserting (3.14), (3.12), and the derivative of (3.6) into (4.13) we obtain

$$S(\delta_\tau) = -\sqrt{\frac{E_s}{T_s}}\mathrm{E}\left\{ \mathrm{Re}\left\{ \sum_{k\in\mathcal{K}_{\mathrm{TED}}} b_{k,n}^{*} \int_{nT_s}^{(n+D_k)T_s} r(t)\dot{g}_k(t-nT_s)dt \right\} \middle| \delta_\tau \right\}.$$

We next insert the received signal (2.7), into the above expression. Since noise is considered to be independent of the data symbols, we can further simplify to obtain the

following expression

$$S(\delta_\tau) = -\frac{E_s}{T_s} \sum_{k \in \mathcal{K}_{\text{TED}}} \int_{nT_s}^{(n+D_k)T_s} \sum_{q=0}^{N-1} \sum_{i=\left\lfloor \frac{t-\delta_\tau}{T_s} \right\rfloor - D_q + 1}^{\left\lfloor \frac{t-\delta_\tau}{T_s} \right\rfloor} A_{q,k}(n-i) g_q(t - \delta_\tau - iT_s) \dot{g}_k(t - nT_s)\, dt \tag{A.1}$$

where

$$A_{q,k}(n-i) \triangleq \mathrm{E}\left\{ b_{q,i} b_{k,n}^* \right\}$$

is the real-valued cross-correlation function of the pseudo-symbols and is given in closed-form in [3]. The limits for the summation on i are $\lfloor x \rfloor$ denotes the largest integer value of x not exceeding x.

A.2 Phase S-Curve

As mentioned previously, the S-curve $S(\delta_\theta)$ determines the loop acquisition properties of the phase PLL. This is defined as the expectation computed under the assumption of correct decision and a fixed known value of phase offset $\delta_\theta = \theta - \hat{\theta}$. To further simplify the analysis we assume $\hat{\theta} = 0$. Then from 3.20, we have

$$S(\delta_\theta) = \sqrt{\frac{E_s}{T_s}} \mathrm{E}\left\{ e_n | \delta_\theta \right\} = \sqrt{\frac{E_s}{T_s}} \mathrm{E}\left\{ \mathrm{Im}\left[\sum_{k \in \mathcal{K}_{\text{PED}}} x_{k,i} b_{k,i}^* e^{-j\delta_\theta} \right] | \delta_\theta \right\} \tag{A.2}$$

Substituting 2.7 into 3.15 and from 3.6 we express $x_{k,i} b_{k,i}^*$ as

$$x_{k,i} b_{k,i}^* = \left[\sum_{m \in \mathcal{K}_{\text{PED}}} \sum_{n} b_{m,n} b_{k,i}^* \rho_{m,k}(i-n) T_s \right] e^{j\delta_\theta} \tag{A.3}$$

where $\rho_{m,k} \triangleq g_m(t) \otimes g_k(-t)$. Assuming noise and data symbol are uncorrelated

and therfore independent (Gaussian noise), expectation taken of the noise, becomes zero.

$$S(\delta_\theta) = \sqrt{\frac{E_s}{T_s}}\text{Im}\left\{\sum_{j\in\mathcal{K}_{\text{PED}}}\sum_{k\in\mathcal{K}_{\text{PED}}}\sum_{n} A_{m,k}(i-n)\rho_{m,k}[(i-n)T_s]e^{j\delta_\theta}\right\} \tag{A.4}$$

where

$$A_{m,k}(i-n) \triangleq \text{E}\left\{b_{m,n}b^*_{k,i}\right\}$$

A.3 General Guidelines for Simulating the S-Curve

The following are a few important steps to simulate an S-curve using MATLAB or other simulation tools.

1. Open the loop filter and run the detectors described as Figure 3.1, Figure 3.2 and Figure 3.3 with known offsets in the corresponding signal attributes and discard the noise introduced in the channel (AWGN).

2. Accumulate the errors from the TED, PED output after each symbol index.

3. Assuming the error generation process is wide sense stationary (WSS), obtain the average of the errors over the total received symbol length.

4. Follow steps 1 to 3 for another known timing or phase offset.

5. Finally, plot the average error against the corresponding offset for the selected range.

Appendix B

Performing Digital Synchronizations

B.1 Digital Sample Interpolation

The problem of timing correction for synchronous sampling is now addressed. We used linear interpolation discussed in [18] to produce synchronized samples based on the timing estimate obtained from the timing PLL after every symbol time. A linear interpolation algorithm is illustrated in Figure B.1 The received discrete-time signal is sampled at a higher sample rate N called the over-sampling factor. Ideally, we would like the sampling pulses to be issued at the instants $t_n = \frac{T_s}{N} + \tau$ for every symbol index k. Therefore, we have to compute $r(kt_n)$ from the available samples of the received signal $r(nT)$ by a technique called "interpolation". Assuming the k-th interpolated sample is between samples $r(nT)$ and $r((n+1)T)$, the sample index is called k-th basepoint index; denoted by $m(k)T$. The time instant kt_n is some fraction $\tau(k)T$ of a sample time greater than $m(k)T$ that satisfies the condition $0 \leq \tau(k) < 1$ and is defined by $\tau(k)T = kt_n - m(k)T$. To produce the samples at the desired instants kt_n, samples of $r(nT)$ are recreated at intervals kt_n.

Linear interpolation is practically performed from a piecewise polynomial inter-

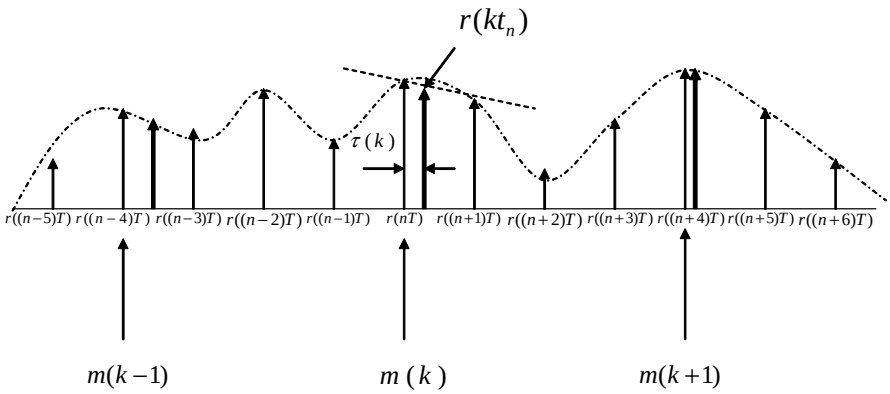

Figure B.1. Linear interpolation overview: relationships between the exact time instant t_n, sample time T, base-point index $m(k)$ and fractional time-delay $\tau(k)$

polation model. With this model, the discrete-time waveform is approximated by the polynomial of order m and sampled at $t = kt_n$ as

$$r(kt_n) \approx h_m(kt_n)^m + h_{m-1}(kt_n)^{m-1} + \cdots + h_1(kt_n) + h_0 \tag{B.1}$$

The polynomial or the FIR filter coefficients h_m are obtained easily using a first-order piecewise polynomial approximation, so that B.1 is reduced to

$$r(kt_n) \approx h_1(kt_n) + h_0 \tag{B.2}$$

Therefore, the desired samples at the instants $t = kt_n$ are computed from

$$r((m(k) + \tau(k))T) = h_1((m(k) + \tau(k))T) + h_0 \tag{B.3}$$

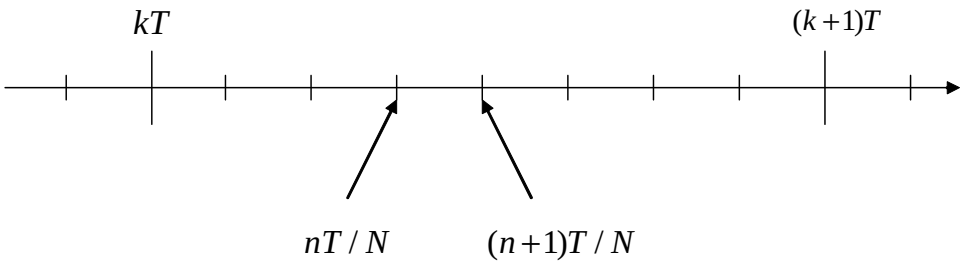

Figure B.2. Digital integration of phase

The coefficients h_1 and h_0 are computed from the equation descried in [18, p. 465, eq. 8.60]

$$\begin{bmatrix} r(m(k)T) \\ r((m(k)+1)T) \end{bmatrix} = \begin{bmatrix} r(m(k)T) & 1 \\ r((m(k)+1)T) & 1 \end{bmatrix} + \begin{bmatrix} h_1 \\ h_0 \end{bmatrix} \tag{B.4}$$

Solving for h_1 and h_0 and substituing their values into B.3 we obtain

$$r((m(k)+\tau(k))T) = \tau(k)r((m(k)+1)T) + (1-\tau(k))r(m(k)T) \tag{B.5}$$

which is the equation of a linear interpolator.

B.2 Digital Integration of Phase

We discuss here the algorithm for derivation of integration operation on the phase $\Phi(nT)$ described in Section 3.3 To do that, we first divide the interval $kT_s \leq t \leq (k+1)T_s$ into N sub-intervals of length $T = T_s/N$ as shown in B.2. The digital integration is performed over a subinterval $nT \leq t \leq (n+1)T$ yielding

$$\Phi\left[(n+1)T\right] = \Phi(nT) + 2\pi\tilde{\nu}(kT)T_s/N \tag{B.6}$$

The above equation involves two indexes: A sample index n and a symbol index k.

From Figure B.2 they are related by $k = \text{int}(\frac{n}{N})$. where int$(m)$ represents the largest integer not exceeding m. Practically, to limit the overflow while computing (B.6), Φ modulo 2π is taken. Therefore, (B.6) is expressed as

$$\Phi\left[(n+1)T\right] = \Phi(nT) + 2\pi\tilde{\nu}(kT)T_s/N \mod 2\pi \tag{B.7}$$

Appendix C

Laurent Decomposition of CPM and Approximation of the PAM pulses

In this chapter, we present the *Laurent* decomposition of CPM pulses used in this thesis to explain the *joint* frequency, timing and phase recovery algorithms and false lock recovery for M-ary CPMs.

C.1 Binary GMSK System with Gaussian Pulses: $M = 2$, $h = 1/2$, $L = 4$

In this case, Laurent decomposition with $L = 4$ will give $Q^P(2^P - 1) = 8$ PAM pulses according to [3], where $Q = 2^L - 1$ and $P = \log_2(M)$.

Figure C.1 shows that out of these 8 pulses only pulse marked as $g_0(t)$ and $g_1(t)$ have significant energies. Therefore, we select only 2 PAM pulses for using as the matched filter responses. For TED, PED and FDD however we can select only $g_0(t)$ without degrading the acquisition and tracking performances too much.

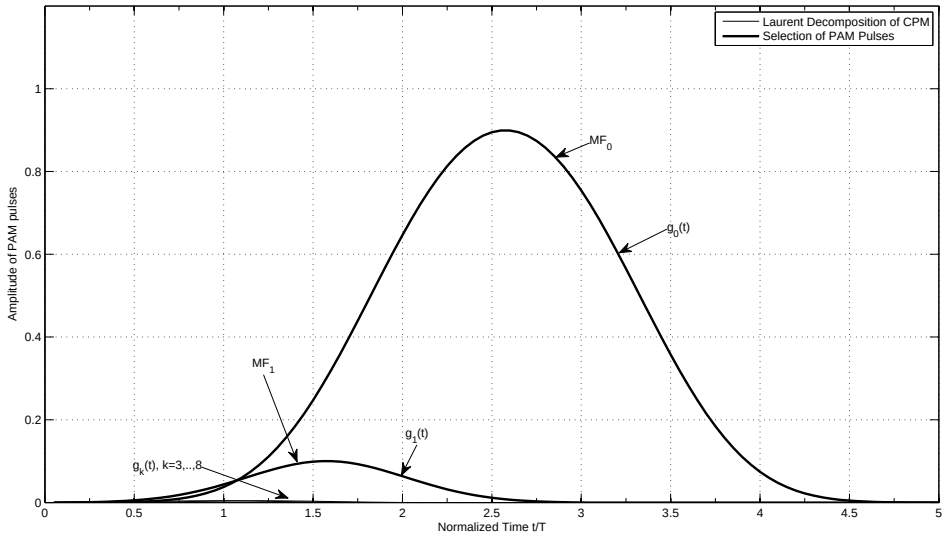

Figure C.1. Laurent decomposition of binary GMSK with $M = 2$, $L = 4$ and $h = 1/2$

C.2 M-ary Partial Response System with $M = 4$, $h = 1/4$, 2RC

We now have, after the Laurent decomposition, $Q^P(2^P - 1) = 12$ PAM pulses according to [3], where $Q = 2^L - 1$ and $P = \log_2(M)$.

Figure C.2 shows that, out of these 12 pulses, only 3 pulses, marked as $g_0(t)$, $g_1(t)$ and $g_2(t)$ have significant energies. To reduce the MF pulse requirement in this case, we select only 2 PAM pulses for using as the matched filter response. While selecting the pulses, we observe that, $g_1(t)$ and $g_2(t)$ have almost the same energy. We use a simple average of these two similar energy pulses for the second MF response. We select only $g_0(t)$ for the error detection pupose.

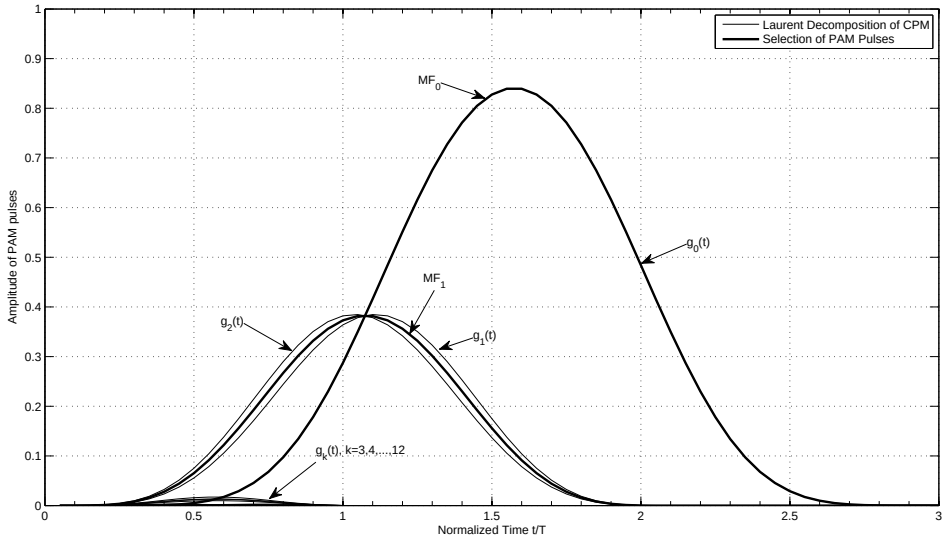

Figure C.2. Laurent decomposition of the quaternary CPM with $M = 4$, $L = 2$ and $h = 1/4$

C.3 M-ary Partial Response System with $M = 4$, $h = 1/2$, 3RC

We now have, after the Laurent decomposition, $Q^P(2^P - 1) = 12$ PAM pulses according to [3], where $Q = 2^L - 1$ and $P = \log_2(M)$.

This case is different than the previous two as the Laurent decomposition generates a product of two binary signals with modulation indexes $1/2$ and 1. As we know that Laurent decomposition doesn't work for integer modulation indexes, so we use the method described in [5]. So instead of $Q^P(2^P - 1) = 48$ predicted by Laurent, actually we get 17 PAM pulses.

Figure C.3 shows that, out of these 17 pulses, only 3 pulses, marked as $g_0(t)$, $g_1(t)$ and $g_2(t)$ have significant energies. For the reduced MF pulse requirement in this case, we take only 2 PAM pulses for using as the matched filter response. We also make note of the fact that, $g_1(t)$ and $g_2(t)$ have comparable energies than other low energy pulses. Therefore, we use a simple average of these two energy pulses for the second MF

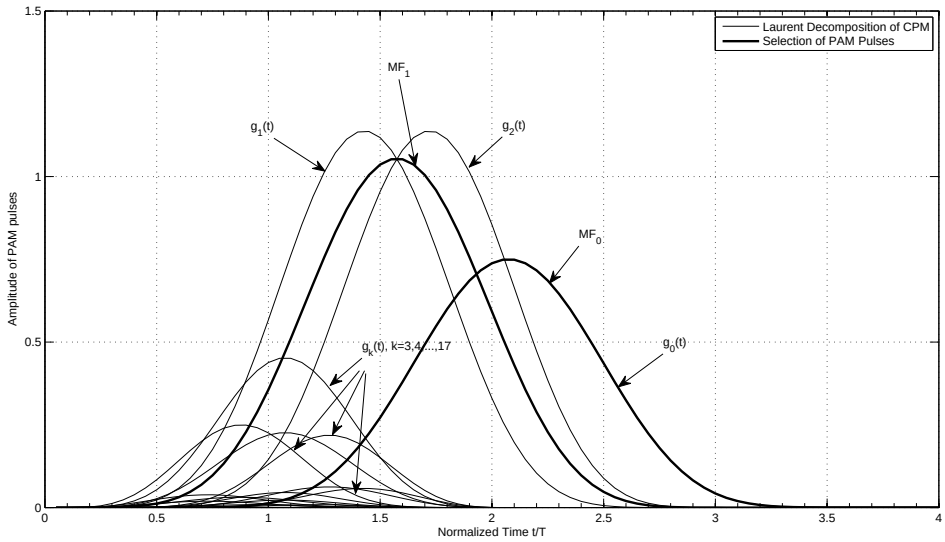

Figure C.3. Laurent decomposition of the quaternary CPM with M=4, L=3 and h=1/2

response. Again, for the TED, the PED and the FDD, selecting only $g_0(t)$ is sufficient in most cases. In fact, as this scheme is a M-ary partial-response, selecting only $g_0(t)$ for the error detectors is beneficial in avoiding the false lock problem mentioned in Chapter 7.

References

[1] J. B. Anderson, T. Aulin, and C.-E. Sundberg, *Digital Phase Modulation*. New York: Plenum Press, 1986.

[2] P. A. Laurent, "Exact and approximate construction of digital phase modulations by superposition of amplitude modulated pulses (AMP)," *IEEE Trans. Commun.*, vol. 34, pp. 150–160, Feb. 1986.

[3] U. Mengali and M. Morelli, "Decomposition of M-ary CPM signals into PAM waveforms," *IEEE Trans. Inform. Theory*, vol. 41, pp. 1265–1275, Sep. 1995.

[4] E. Perrins and M. Rice, "PAM decomposition of M-ary multi-h CPM," *IEEE Trans. Commun.*, vol. 53, pp. 2065–2075, Dec. 2005.

[5] X. Huang and Y. Li, "The PAM decomposition of CPM signals with integer modulation index," *IEEE Trans. Commun.*, vol. 51, pp. 543–546, Apr. 2003.

[6] M. P. Wylie-Green, "A new finite series expansion for continuous phase modulated waveform," *IEEE Trans. Commun.*, vol. 55, pp. 1547–1556, Aug. 2007.

[7] G. K. Kaleh, "Simple coherent receivers for partial response continuous phase modulation," *IEEE J. Sel. Areas Commun.*, vol. 7, pp. 1427–1436, Dec. 1989.

[8] G. Colavolpe and R. Raheli, “Reduced-complexity detection and phase synchronization of CPM signals,” *IEEE Trans. Commun.*, vol. 45, pp. 1070–1079, Sep. 1997.

[9] E. Perrins and M. Rice, “A new performance bound for PAM-based CPM detectors,” *IEEE Trans. Commun.*, vol. 53, pp. 1688–1696, Oct. 2005.

[10] A. N. D’Andrea, A. Ginesi, and U. Mengali, “Frequency detectors for CPM signals,” *IEEE Trans. Commun.*, vol. 43, pp. 1828–1837, Feb./Mar./Apr. 1995.

[11] A. N. D’Andrea, U. Mengali, and M. Morelli, “Symbol timing estimation with CPM modulation,” *IEEE Trans. Commun.*, vol. 44, pp. 1362–1372, Oct. 1996.

[12] M. Morelli, U. Mengali, and G. M. Vitetta, “Joint phase and timing recovery with CPM signals,” *IEEE Trans. Commun.*, vol. 45, pp. 867–876, Jul. 1997.

[13] Q. Zhao and G. L. Stuber, “Joint time and phase recovery for cpm and its asymptotic behavior,” in *Proc. IEEE. GLOBECOM.*, 2005.

[14] M. Morelli and G. Vitetta, “Joint phase and timing recovery for MSK-type signals,” *IEEE Trans. Commun.*, vol. 48, Dec. 2000.

[15] J. G. Proakis and M. Salehi, *Digital Communications*. New York: McGraw-Hill Science/Engineering/Math, 2007.

[16] E. Perrins and B. Kumaraswamy, “Decision feedback detectors for SOQPSK,” *IEEE Trans. Commun.*, vol. 57, Aug. 2009.

[17] E. Perrins, S. Bose, and M. P. Wylie-Green, “Timing recovery based on the PAM representation of CPM,” in *Proc. IEEE Military Communications. Conf.*, Nov. 2008.

[18] M. Rice, *Digital Communications - A Discrete-Time Approach*. New Jersey: Prentice Hall, 1986.

[19] A. N. D'Andrea, U. Mengali, and R. Reggiannini, "The modified Cramer-Rao bound and its application to synchronization problems," *IEEE Trans. Commun.*, vol. 42, pp. 1391–1399, Feb./Mar./Apr. 1994.

[20] U. Mengali and A. N. D'Andrea, *Synchronization Techniques for Digital Receivers*. New York: Plenum Press, 1997.